

---

## **Suche nach Elektroweakinos mit dem ATLAS Detektor**

---



LUDWIG-MAXIMILIANS-UNIVERSITÄT MÜNCHEN  
FAKULTÄT FÜR PHYSIK

DISSERTATION

Eric Schanet  
March 2021

Supervisor: PD Dr. Jeanette Lorenz



# Notes

Natural units and Minkowski metric . . . . .	3
Couplings and masses are measured from experiment . . . . .	8
Write somewhere SU2xU1 to U1 breakdown . . . . .	18
Mass dimension needs to be $< 4$ . . . . .	19
DM relic density . . . . .	20
Mention link to gravity . . . . .	25
Reference, why? . . . . .	36
is this true? . . . . .	51
simulation tools allow to plugin any Lagrangian and get events at detector level . . . . .	52
MCViz signal event? . . . . .	55
Explain this further . . . . .	58
refer to observables . . . . .	67
truth jets . . . . .	74
Need presel plots for these . . . . .	85
is this conf up-to-date? . . . . .	86
prefit plots of VR? . . . . .	99
Plots from HF numbers? . . . . .	108
quote exact numbers . . . . .	113
cite . . . . .	122
some examples . . . . .	128



# Part I

## Fundamental concepts



# Chapter 2

# Experiment

One of Europe’s first joint ventures in science [82], CERN (*Conseil Européen pour la Recherche Nucléaire*) is the largest physics research facility in the world, bringing together more than 12,400 scientists of over 110 nationalities [83] with a common goal of pushing the frontiers of science and technology. Located at the Franco-Swiss border near Geneva, CERN was founded in 1954 and nowadays counts 23 member states [83]. CERN’s main research area is particle physics, hence why the organisation operates a large complex of particle accelerators and detectors.

This chapter introduces the Large Hadron Collider (LHC), CERN’s main particle accelerator, as well as the ATLAS experiment, in which the search for Supersymmetry (SUSY) presented in this work is embedded in.

## 2.1 The Large Hadron Collider

The LHC [84] is the largest particle accelerator situated at CERN. It is installed in a tunnel with 26.7 km circumference, that was originally constructed from 1984 to 1989 for the Large Electron Positron (LEP) accelerator. The tunnel is situated on the Franco-Swiss border and wedged between the Jura mountains and lake Léman. It lies between 45 m (in the limestone of the Jura) and 170 m (in molasse rock) below the surface, resulting in a tilt of 1.4% towards the lake. While proton-proton ( $pp$ ) collisions are the main operating mode of the LHC, its design also allows it to accelerate and collide heavy ions like lead and xenon. Since data from  $pp$  collisions is used in this work, the following sections will mainly focus on this operating mode. As a particle-particle collider, the LHC obviously consists of two rings with counter-rotating beams, as opposed to particle-antiparticle colliders that only need a single ring. With an inner diameter of only 3.7 m, the tunnel however simply too narrow to fit two separate proton rings. Instead the LHC is built in a twin bore design<sup>†</sup>, housing two sets of coils and beam channels in a single magnetic and mechanical structure and cryostat [84]. While saving costs, this design has the disadvantage of both beams being magnetically coupled, thereby reducing flexibility of the machine.

---

<sup>†</sup> Originally proposed by John Blewett at BNL for cost-saving measures of the Colliding Beam Accelerator [85, 86].

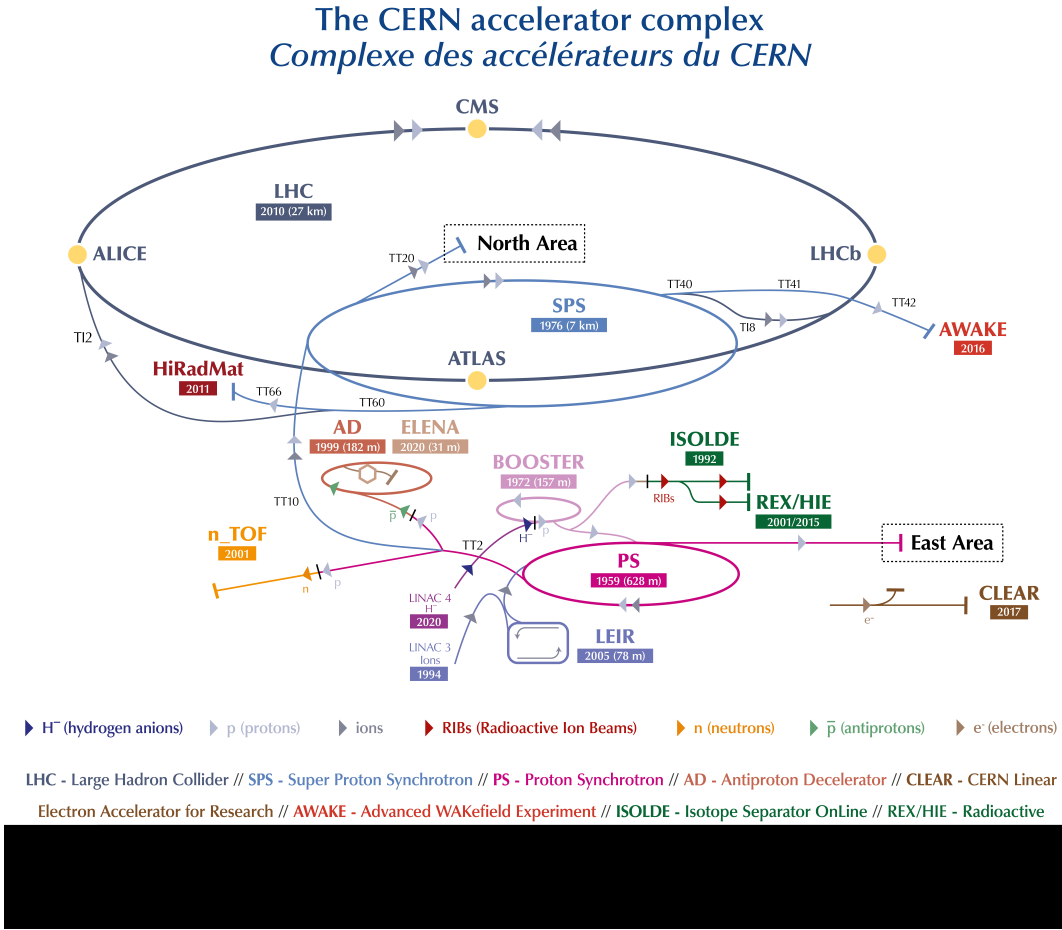


Figure 2.1: CERN accelerator complex as of 2018 [88].

Before being injected into the LHC, protons are pre-accelerated by an injection chain built from multiple existing machines in CERN's accelerator complex, pictured in fig. 2.1. The injection chain consists of predecessor accelerators that have been upgraded in order to be able to handle the high luminosity and high energy requirements of the LHC. The protons for the LHC stem from a duoplasmatron source [87], stripping electrons from hydrogen atoms through electric discharges between a hot anode and cathode. The 90 keV protons are then accelerated by a radio frequency (RF) quadrupole to 750 keV before being injected into Linac2<sup>†</sup>, a linear accelerator producing a beam of 50 MeV protons through the use of RF cavities. The protons then enter a set of circular accelerators, the Proton Synchrotron Booster, the Proton Synchrotron and the Super Proton Synchrotron, creating a stepwise acceleration up to an energy of 450 GeV, which is the injection energy of the LHC. The LHC finally accelerates the protons up to nominal beam energy before colliding them.

The LHC is composed of eight straight sections and eight arcs. The eight straight sections each serve as interaction points (*Point*), either for particle detectors, or for machine hardware of the

<sup>†</sup> Originally built to replace Linac 1 in order to produce higher energetic proton beams, Linac 2 has been replaced by Linac 4 in 2020.

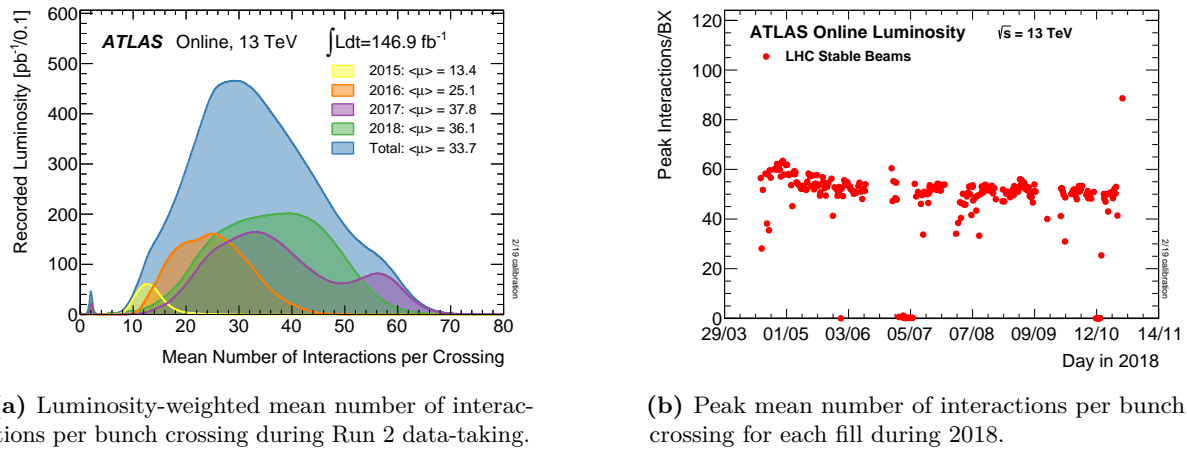
collider itself. The Points are labelled clockwise, with IP 1 being closest to the CERN Meyrin site. Four of the eight Points house the main particle physics experiments at the LHC, called ATLAS, CMS, ALICE and LHCb, covering a wide range of fundamental research. The two general purpose particle detectors ATLAS [89] and CMS [90] are installed at Point 1 and Point 5, respectively. Both ATLAS and CMS are designed to perform high precision SM measurements including Higgs measurements as well as searches for BSM physics. Being very similar in terms of targeted phase space, ATLAS and CMS can be used to cross-check results of each other. ALICE [91] is situated at Point 2 and specializes on heavy ion physics, studying the physics of quark-gluon plasma at high energy densities. Built in Point 8, LHCb [92] targets  $B$ -physics and performs measurements of CP-violation. Apart from the four main experiments, three smaller experiments exist at the LHC: TOTEM, MoEDAL and LHCf. While TOTEM [93] and LHCf [94] study forwards physics close to CMS and ATLAS, respectively, MoEDAL [95] searches for magnetic monopoles.

The remaining four Points house accelerator equipment needed for operation of the LHC. Most of the collimation system is placed at Point 3 and Point 7, performing beam cleaning and machine protection through a series of beam intercepting devices, ensuring that no stray particles from experimental debris or beam halo can reach and damage other machine components. The acceleration of the beam itself is performed at Point 4 with two RF systems, one for each LHC beam. The RF cavities operate at 400 MHz and provide 8 MV during injection and 16 MV during coast [84]. Due to the RF acceleration, the accelerated protons are grouped in packages called *bunches*, each containing roughly  $10^{11}$  protons, with a bunch spacing of 25 ns [84]. Each beam contains a total of 2808 [84] bunches as design value. The remaining Point 6 houses the beam dumping system, allowing to horizontally deflect and fan out both beams into dump absorbers using fast-paced *kicker* magnets. The two nitrogen-cooled dump absorbers each consist of a graphite core contained in a steel cylinder, surrounded by 750 t [84] of concrete and iron shielding. Insertion of the beams from the Super Proton Synchrotron into the LHC happens at Points 2 and 8, close to the ALICE and LHCb experiments.

The eight arcs of the LHC are filled with dipole magnets built from superconducting NbTi Rutherford cables. The electromagnets are responsible for keeping the accelerated particles on their circular trajectory and are the limiting factor of the maximal centre-of-mass energy,  $\sqrt{s}$ , of the LHC. In order to achieve the design energy of  $\sqrt{s} = 14$  TeV [84], the magnets have to create a field strength of 8.3 T [84]. In order to sustain the electric currents needed for such high field strengths, the magnets need to be cooled down to 1.9 K [84] using superfluid helium and operated in superconducting state. In addition to the dipole magnets, the arcs contain quadrupole magnets used to shape and focus the beams, as well as multipole magnets correcting and optimizing the beam trajectory. Quadrupole magnets are also used to reduce the beam size before and after the interaction points.

### 2.1.1 Pile-up

Due to the high number of protons in each bunch, several  $pp$  collisions occur at each bunch crossing. This leads to a phenomenon called *pile-up*, where the recorded events not only contain information from the hard-scattering process of interest, but also remnants from additional, often low-energy,  $pp$  collisions. During the Run 2 data-taking period, the mean number of inelastic  $pp$  collisions per bunch crossing,  $\mu$ , has varied from roughly 10 to 70, with the majority



(a) Luminosity-weighted mean number of interactions per bunch crossing during Run 2 data-taking.

(b) Peak mean number of interactions per bunch crossing for each fill during 2018.

**Figure 2.2:** Number of interactions per bunch crossing recorded by the ATLAS detector [96]

of bunch crossings having a value of  $\mu$  around 30. Figure 2.2(a) shows the mean number of interactions per bunch crossing during the Run 2 data-taking period, weighted by luminosity. The peak number of interactions per bunch crossing  $\mu_{\text{peak}}$  per fill has been consistently around 50 during the 2018 data-taking (cf. fig. 2.2(b)).

Experimentally, pile-up can be divided into five major components [97]:

- *In-time* pile-up: multiple interactions during a single bunch crossing, of which not all will be interesting, as often with relatively low energy. If they can be resolved, the main hard-scattering event can still be isolated and studied.
- *Out-of-time* pile-up: additional collisions occurring in bunch crossings before or after the main event of interest. This happens either due to read-out electronic integrating over longer time frames than the 25 ns bunch spacing, or detector components being sensitive to several bunch crossings.
- *Cavern background*: gas of thermal neutrons and photons that typically fill the experimental caverns during a run of the LHC and tend to cause random hits in detector components.
- *Beam halo events*: protons scraping an up-stream collimator, typically resulting in muons travelling parallel to the beam pip
- *Beam gas events*: collision events that originate from interactions between proton bunches and residual gas inside the beam pipe.

While the effects of cavern background can be mitigated through special pieces of shielding, beam halo and beam gas events leave signatures that can be recognized and removed. Signals from in-time and out-of-time pile-up create irreducible overlap with the events of interest, significantly impacting analyses, and thus need to be simulated [97].

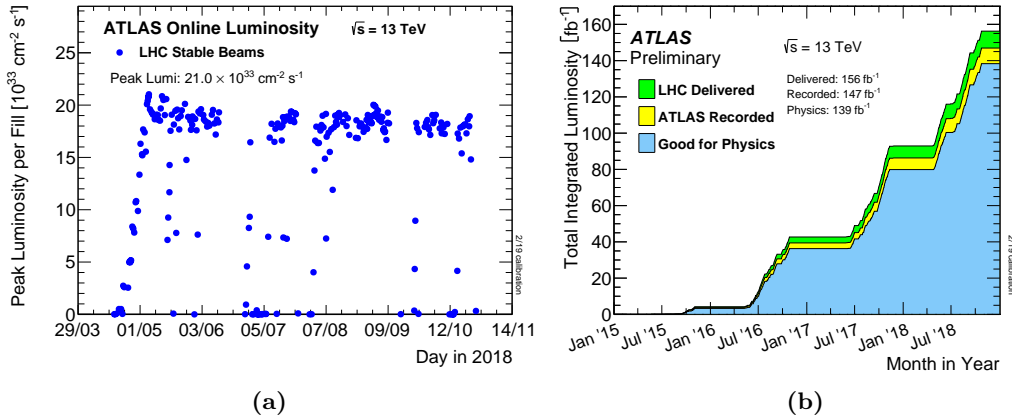


**Figure 2.3:** Instantaneous and cumulative luminosities in Run 2. Figure (a) shows the peak instantaneous luminosity delivered to ATLAS during  $pp$  collision data taking in 2018 as a function of time. Figure (b) shows the cumulative luminosity delivered to ATLAS (green), recorded by ATLAS (yellow) and deemed good for physics analysis (blue) during the entirety of Run 2 [96].

### 2.1.2 Luminosity and data-taking

Apart from the beam energy, the most important quantity for a collider is the instantaneous luminosity  $L$ . For a synchrotron with Gaussian beam distribution, the instantaneous luminosity can be written as

$$L = \frac{N_b^2 n_b f_{\text{rev}}}{4\pi\sigma_x\sigma_y} F, \quad (2.1)$$

where  $n_b$  is the number of bunches,  $N_b$  the number of protons per bunch,  $f_{\text{rev}}$  the revolution frequency and  $\sigma_x$  and  $\sigma_y$  the transverse beam sizes. The parameters  $F$  is a geometrical correction factor accounting for the reduction in instantaneous luminosity due to the beams crossing at a certain crossing angle. While the design instantaneous luminosity of the LHC at the high-luminosity experiments ATLAS and CMS is  $L = 10^{34} \text{ cm}^{-2} \text{ s}^{-1}$  [86], the 2017 and 2018 data-taking periods saw a peak luminosity twice as high [98].

The instantaneous luminosity is related to the total number of events  $N$  through the cross section  $\sigma$  of the events in question

$$N = \sigma L_{\text{int}} = \sigma \int L dt, \quad (2.2)$$

with  $L_{\text{int}}$  the total integrated luminosity, a measure for the total amount of collision data produced.

A precise knowledge of the integrated luminosity corresponding to a given dataset is crucial for both SM measurements as well as searches for beyond the Standard Model (BSM) physics. Searches for SUSY like the one presented in this work rely on precise measurements of the integrated luminosity in order to be able to estimate the contribution from SM background processes. The luminosity measurement for the Run 2 dataset used within this work is described in detail in [99, 100] and relies on a measurement of the bunch luminosity, i.e. the luminosity

produced by a single pair of colliding bunches

$$L_b = \frac{\mu f_{\text{rev}}}{\sigma_{\text{inel}}} = \frac{\mu_{\text{vis}} f_{\text{rev}}}{\sigma_{\text{vis}}}, \quad (2.3)$$

with  $\mu$  the pile-up parameter,  $\sigma_{\text{inel}}$  the cross section of inelastic  $pp$  collisions,  $\mu_{\text{vis}} = \epsilon\mu$  is the fraction  $\epsilon$  of the pile-up parameter  $\mu$  visible to the detector and  $\sigma_{\text{vis}} = \epsilon\sigma_{\text{inel}}$  the visible inelastic cross section. If  $\sigma_{\text{vis}}$  is known, the currently recorded luminosity can be determined by measuring  $\mu_{\text{vis}}$ . At the ATLAS experiment, the observed number of inelastic interactions per bunch crossing  $\mu_{\text{vis}}$  is measured using dedicated detectors, as for example LUCID-2 [101], a forward Cherenkov-detector using the quartz windows from photomultipliers as Cherenkov medium. In order to use  $\mu_{\text{vis}}$  as luminosity monitor, the respective detectors need to be calibrated through a measurement of the visible inelastic cross section  $\sigma_{\text{vis}}$ . This can be done using van der Meer (vdM) scans [102, 103], in which the transverse distribution of protons in the bunches is inferred by measuring the relative interaction rates as a function of the transverse beam separation<sup>†</sup>. The algorithms used to determine the  $\sigma_{\text{vis}}$  calibration are described in [99, 100] and the luminosity during the vdM runs can be determined using eq. (2.1). At the LHC, vdM scans are typically performed in special low- $\mu$  runs with well-known machine parameters in order to minimise uncertainties [99]. During high- $\mu$  physics runs, the luminosity measurement is then an extrapolation from the vdM runs.

The LHC entered operation in 2008, with first beams in September and first collisions by the end of November that same year [104]. Its operation is in general structured into so-called *Runs*, that are spanned by multiple years of data-taking. Run 1 spanned from 2009 to 2013 and delivered roughly  $28.5 \text{ fb}^{-1}$  of  $pp$  collision data to ATLAS, taken at centre-of-mass energies of 7 TeV and 8 TeV [105, 106, 100]. Run 2 lasted from 2015 to 2018 and saw a centre-of-mass energy increase to 13 TeV, delivering approximately  $156 \text{ fb}^{-1}$  of  $pp$  collision data to ATLAS [99]. Run 3 of  $pp$  collision data taking with two times design peak luminosity is currently planned to start its physics program in 2022 and last until end of 2024 [107]. Current plans foresee Run 3 to deliver about  $150 \text{ fb}^{-1}$  of  $pp$  collision data with centre-of-mass energies of 13 TeV and 14 TeV. After Run 3, the LHC will be upgraded to the High Luminosity LHC, significantly increasing the peak instantaneous luminosity and delivering up to  $3000 \text{ fb}^{-1}$  of  $pp$  collision data from 2027 until 2040 [107, 108].

This work uses  $pp$  collision data taken by ATLAS during Run 2 of the LHC. Of the  $156 \text{ fb}^{-1}$  delivered to ATLAS,  $147 \text{ fb}^{-1}$  were recorded, and  $139 \text{ fb}^{-1}$  were deemed to be good for physics analysis. Figure 2.3 shows the cumulative luminosity delivered to ATLAS during Run 2. Uncertainties on the measurement total recorded luminosity stem from the measurements of  $\mu_{\text{vis}}$  and  $\sigma_{\text{vis}}$ , but are dominated by the uncertainties on  $\sigma_{\text{vis}}$  as vdM scans can only be done during special runs, while the general conditions during high- $\mu$  conditions change continuously. For the full Run 2 dataset, the uncertainties accumulate to  $\pm 1.7\%$  [99].

## 2.2 ATLAS Experiment

The ATLAS experiment is one of two general-purpose detectors at the LHC. Located at Point 1 in a cavern 100 m below the surface, it is approximately 44 m long and 25 m high [89]. The

---

<sup>†</sup> Often called *beam sweeping*.

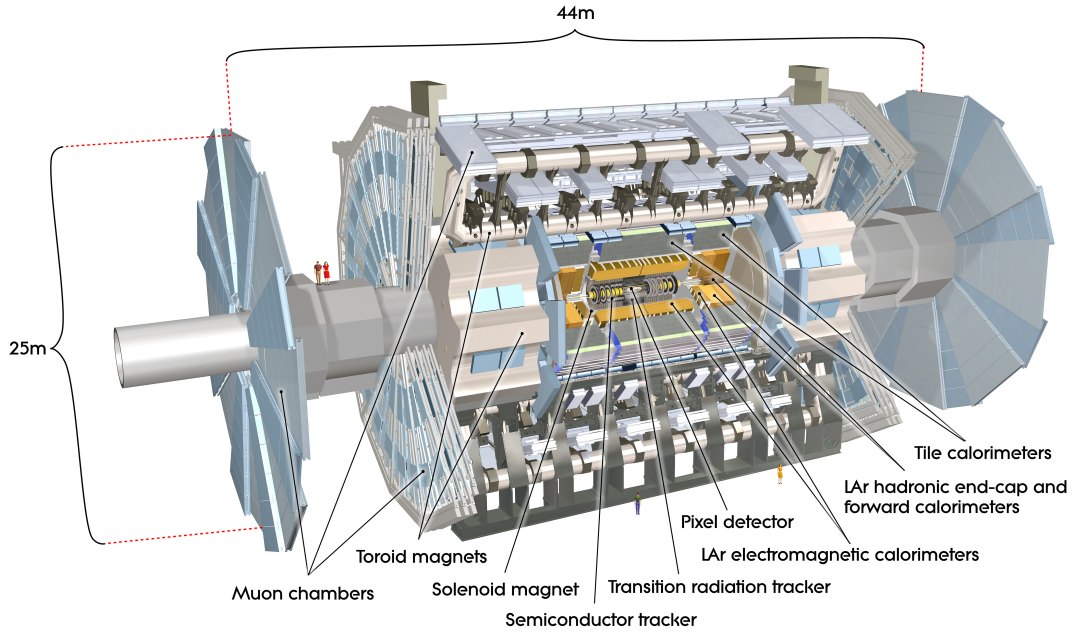


**Figure 2.4:** Computer generated picture of the ATLAS detector, giving an overview on the various subsystems [109].

design of the ATLAS experiment is driven by the aim to allow for a diverse research program, including SM precision measurements, Higgs physics and searches for BSM physics, whilst at the same time taking into account the unique and challenging conditions set by the LHC. The various detector technologies used are designed to withstand the high-radiation environment of the LHC, while allowing particle measurements with high spatial and temporal granularity. The general structure of ATLAS is depicted in fig. 2.4, and consists of a central part, called *barrel*, that has a cylindrical shape around the beam pipe, and two discs, called *end-caps*, that close off the barrel on each side. This makes the ATLAS detector forward-backward symmetric and covering nearly the full solid angle of  $4\pi$ , which is needed in order to measure momentum imbalances caused by particles that only interact weakly with the detector material.

The interface between the ATLAS experiment and the LHC is the beam pipe. In order to be maximally transparent to the particles created in the collisions, but also be able to withstand the forces from the vacuum, the beam pipe is made out of Beryllium close to the interaction point (IP), and stainless-steel further away from the IP [1].

The following sections introduce the working principles of the different detector components used in ATLAS, starting with the innermost component closest to the IP, the inner detector, followed by the calorimeters in the middle and finally the muon spectrometers on the outside. If not otherwise stated, details on the detector components are extracted from [89].

### 2.2.1 Coordinate system

In order to properly describe collision events in the ATLAS detector, a suitable detector system is needed. The right-handed coordinate system [110] used in ATLAS has its origin at the nominal IP in the centre of the detector. The positive  $x$ -axis points towards the centre of the LHC ring, the positive  $y$ -axis points upwards to the surface, and the beam pipe is used to define the  $z$ -axis. In the  $x-y$  plane, called the transverse plane, the azimuthal angle  $\phi$  is the angle around the beam axis, and the polar angle  $\theta$  is measured from the beam axis. The rapidity [7] is defined as

$$y = \frac{1}{2} \ln \left( \frac{E + p_z}{E - p_z} \right) = \tanh \frac{p_z}{E}^{-1}, \quad (2.4)$$

with  $E$  the energy of an object and  $p_z$  its momentum in  $z$ -direction. As opposed to the polar angle  $\theta$ , differences in the rapidity are invariant under Lorentz boosts in  $z$ -direction.

The pseudorapidity [7] is the high-energy limit ( $p \gg m$ ) of the rapidity, and defined as

$$\eta = -\ln \tan \frac{\theta}{2}, \quad (2.5)$$

with  $\cos \theta = p_z/p$ . Pseudorapidity and rapidity are approximately equal in the limit where  $p \gg m$  and  $\theta \gg \frac{1}{\gamma}$ . Compared to the rapidity, the pseudorapidity has the advantage of not depending on the energy and momentum calibration of the detected objects. Additionally, it gives a direct correspondence to the polar angle  $\theta$  through the relation  $\tanh \eta = \cos \theta$ . Objects travelling along the beam axis have a pseudorapidity of  $\eta = \text{inf}$  and objects travelling upwards along the  $y$ -axis have  $\eta = 0$ .

The distance between two objects in the ATLAS detector is given by

$$\Delta R = \sqrt{(\Delta\eta)^2 + (\Delta\phi)^2}. \quad (2.6)$$

The longitudinal momentum of the partons composing the colliding hadrons is only known by means of the Parton Distribution Functions (PDFs), giving the probabilities of the partons to have a certain energy in the direction of the beam. Thus, the total longitudinal energy in each collision is not exactly known, impeding the use of physics quantities in the  $z$ -direction. In the  $x-y$  plane, however, momentum conservation can be applied, which is why mainly transverse physics quantities are used, indicated by a subscript ‘T’, e.g.  $E_T$  or  $p_T$ .

### 2.2.2 Magnet system

In order to perform precise momentum measurements of particles, ATLAS uses a system of magnets, whose magnetic fields force charged particles on curved tracks due to the Lorentz force. Using precise measurements of the tracks taken in the inner detector and the muon spectrometers, the curvature of the tracks can be determined, allowing an inference of the charge-to-momentum ratio  $q/p$  of charged particles. ATLAS employs a set of four superconducting magnets, one central solenoid, and three toroids, all operating at a nominal temperature of 4.5 K, achieved through a cryogenic system using liquid helium [89].

The solenoid is aligned on the beam axis and provides a 2 T magnetic field for the inner detector [89]. As it is located in front of the calorimeters (as seen from the IP), it is specially

designed to have minimal material thickness in order to avoid influencing the subsequent energy measurements. The solenoid consists of single-layer coils made out of a Nb/Ti conductor and additional aluminum for stability. It operates at a nominal current of 7.73 kA and uses the hadronic calorimeter as return yoke [89].

The toroid magnets consist of a barrel toroid and two end-cap toroids, producing a magnetic field of 0.5 T and 1 T for the muon spectrometers in the barrel and end-caps, respectively<sup>†</sup> [89]. Both barrel and end-cap toroids are made out of Nb/Ti/Cu conductor with aluminum stabilisation, wound into double pancake-shaped coils. The barrel toroid coils are enclosed in eight stainless-steel vacuum vessels in a racetrack-shaped configuration and arranged around the barrel calorimeters with an azimuthal symmetry. In order to withstand the Lorentz forces, the end-cap toroid coils are assembled in eight square units, and bolted and glued together with eight wedges, forming rigid structures. Both end-cap and barrel toroids operate at a nominal current of 20.5 kA [89].

### 2.2.3 Inner detector

Embedded in the magnetic field of the solenoid, the inner detector (ID) measures tracks of charged particles, allowing a determination of their momentum, while also providing crucial information for vertex reconstruction. As the ID is the detector closest to the beam pipe, its components need to be able to withstand the extreme high-radiation environment close to the IP. The ID consists of three subdetectors and uses two different working principles: semiconductor and gaseous detectors. In semiconductor-based tracking detectors, charged particles passing through the detector create a trail of electron-hole pairs that subsequently drift through the semiconductor material and cause electric signals. In gaseous detectors, traversing particles create electron-ion pairs also drift towards metal electrodes and induce electric signals.

Closest to the ID lies the pixel detector, followed by the silicon microstrip tracker (SCT), both of which are made of semiconductors. The SCT is surrounded by the transition radiation tracker (TRT), a gaseous detector. In total, the ID provides tracking and momentum information within  $|\eta| < 2.5$  and down to transverse momenta of nominally 0.5 GeV. A schematic illustration of the ID and its subdetectors is shown in fig. 2.5.

#### Pixel detector

In the high-rate environment directly adjacent to the beam pipe, the only detector technology able to operate and deliver high-precision tracking information are semiconductor detectors segmented into pixels. As opposed to strip detectors, the reduced size of silicon pixel detectors and thus significantly reduced hit rate per readout channel allows pixel detectors to still be operational in the harsh environment close to the IP. In ATLAS, pixels are hybrids of sensors and readout electronics, and were originally arranged in three layers in the barrel and the end-caps with a typical pixel of  $50 \mu\text{m} \times 400 \mu\text{m}$ , covering pseudorapidities up to  $|\eta| < 2.5$ . In order to increase robustness and performance in the high-luminosity environment, a new innermost layer, called the insertable B-layer (IBL), was installed together with a new, smaller

<sup>†</sup> The magnetic field in of the toroid magnets is designed to be higher in the end-caps in order to ensure enough bending power necessary for precise momentum measurements.

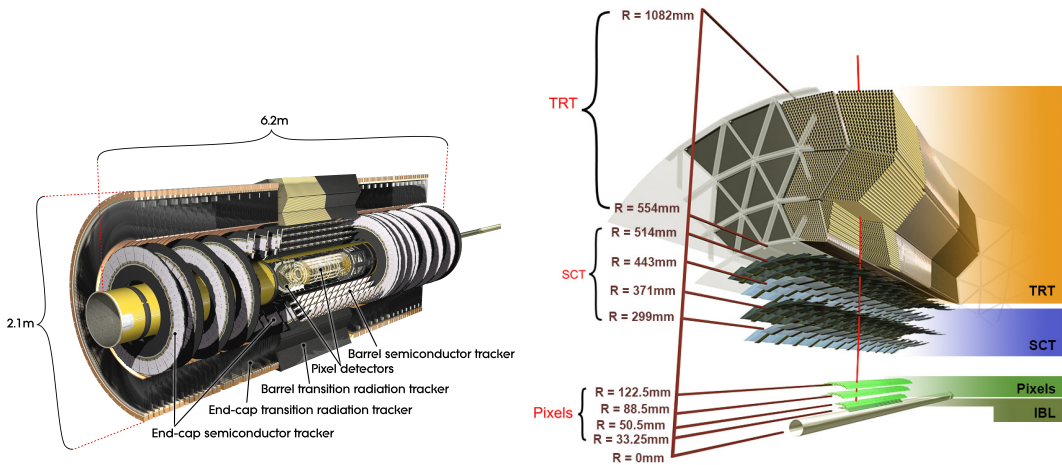


**Figure 2.5:** Schematic drawing of the ID and its subdetectors. Images adapted from [111, 112].

radius beam pipe between Run 1 and Run 2 [113, 114]. The IBL uses smaller pixels with a size of  $50\text{ }\mu\text{m} \times 250\text{ }\mu\text{m}$  and improves the tracking precision as well as vertex identification performance [114]. It also improves the performance of identifying jets originating from  $b$ -quarks (called  $b$ -tagging). The pixel detector [115]. The tracking precision obtained by the pixel detector is  $10\text{ }\mu\text{m}$  in  $(R - \phi)$  and  $115\text{ }\mu\text{m}$  in  $(z)$  for the barrel and  $(R)$  for the end-caps.

### Silicon microstrip detector

The pixel detector is surrounded by the SCT, consisting of four layers in the barrel and nine disks in the end-caps. In order to provide two-dimensional tracking information, strips are arranged in double-layers with a small crossing angle of 40 mrad and a mean pitch of  $80\text{ }\mu\text{m}$  [89]. A charged particle traversing the SCT through the barrel thus creates four space point measurements. In the barrel, one set of strips in each of the four double-layers is oriented in beam direction, thereby measuring  $R - \phi$ , and in the end-caps, one set of strips in each layer is oriented in radial direction. The SCT has roughly 6.3 million readout channels and provides tracking information up to  $|\eta| < 2.5$  [89]. It achieves a precision of  $17\text{ }\mu\text{m}$  in  $(R - \phi)$  and  $580\text{ }\mu\text{m}$  in  $(z)$  for the barrel and  $(R)$  for the end-caps [89].

### Transition radiation tracker

The last and also largest of the three subdetectors of the ID is the TRT, a gaseous detector made of multiple layers of 4 mm diameter drift tubes, surrounding the pixel detector and the SCT. The drift tubes consist of an aluminum cathode coated on a polyimide layer reinforced by carbon fibers and use a gold-plated tungsten wire as anode. The tubes are filled with a Xe-based gas mixture, providing an electric permittivity different from the surrounding material, causing transition radiation when traversed by ultrarelativistic particles. While the 144 cm long tubes in the barrel region are aligned parallel to the beam pipe, the 37 cm long tubes in the end-caps are aligned in radial direction, providing coverage up to  $|\eta| < 2.0$  and an intrinsic accuracy of  $130\text{ }\mu\text{m}$  in  $R - \phi$  [89]. The low accuracy compared to the pixel detector and the SCT is compensated by the large amount of hits (typically 36 per track) and the longer measured

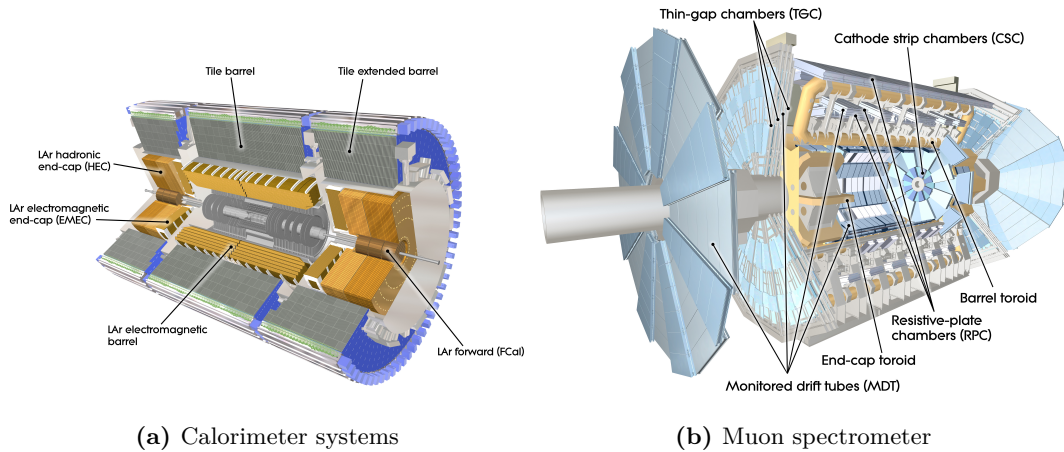


**Figure 2.6:** Schematic drawing of the calorimeter systems and the muon spectrometer in ATLAS. Images adapted from [117, 118].

track length. As the amount of transition radiation given off by a particle, is proportional to its Lorentz factor  $\gamma$  [7], the TRT is also used to improve electron identification [116]. For the same momentum, electrons will have a higher Lorentz factor than the heavier charged pions, and consequently give off more transition radiation.

#### 2.2.4 Calorimeters

The primary goal of calorimeters is to measure the energies of incoming particles by completely absorbing them. As the energies of neutral particles can not be measured by other means, calorimeters are especially important for jet energy measurements (which contain neutral hadrons) [1]. Since particles like photons and electrons interact mostly electromagnetically, while hadrons predominantly interact through the strong interaction, two different calorimeter types are needed in ATLAS. For values in  $\eta$  matching the ID, the electromagnetic calorimeter uses a finer granularity designed for precision measurements of electrons and photons. The subsequent hadronic calorimeter uses a coarser granularity sufficient for the requirements of jet reconstruction and missing transverse moment measurements. With a coverage up to  $|\eta| < 4.9$ , the calorimeter system in ATLAS provides the near hermetic energy measurements needed for the inference of missing transverse momentum created by neutrinos and other weakly interacting neutral particles [89].

Both calorimeters are sampling calorimeters, consisting of alternating layers of active and absorbing material. The absorbing material interacts with the incoming particles, causing them to deposit their energy by creating cascades or *showers* of secondary particles. The active layers are then used to record the shape and intensity of the produced showers. This alternating structure results in reduced material costs but also reduced energy resolution as only part of the particle's energy is sampled. Due to the typically longer cascades in hadronic interactions compared to electromagnetic interactions, and in order to minimise punch-through into the muon system, the hadronic calorimeter requires a greater material depth than the electromagnetic one. The calorimeter systems in ATLAS are schematically illustrated in fig. 2.6(a).

## Electromagnetic calorimeter

The Electromagnetic (EM) calorimeter has an accordion-shaped structure and uses liquid argon (LAr) as active material and lead as absorber, providing full  $\phi$  symmetry without azimuthal cracks. It is divided into a barrel part and two end-caps, covering  $|\eta| < 1.475$  and  $1.375 < |\eta| < 3.2$ , respectively, and arranged in a way to provide uniform performance and resolution as a function of  $\phi$ . The barrel EM calorimeter consists of two identical half-barrels with a small gap of 4 cm at  $z = 0$ . In the end-caps, the EM calorimeter consists of two coaxial wheels, covering the region  $1.375 < |\eta| < 2.5$  and  $2.5 < |\eta| < 3.2$ , respectively. Calorimeter cells in the EM calorimeter are segmented into multiple layers with fine granularity in first layers in the  $\eta$  region matching the ID, and coarser granularity in the outer layers and for  $2.5 < |\eta| < 3.2$ . In order to offer good containment of electromagnetic showers, the EM calorimeter has a depth of at least 22 (24) radiation lengths in the barrel (end-caps). A single instrumented LAr layer serves as presampler in the region with  $|\eta| < 1.8$ , allowing measurements of the energy losses upstream of the EM calorimeter, e.g. in the cryostats [89]. The design energy resolution of the EM calorimeter is  $\sigma_E/E = 10\%/\sqrt{E} \oplus 0.7\%$  [89].

## Hadronic calorimeter

Placed directly outside the envelope of the EM calorimeter is the hadronic tile calorimeter. It uses steel plates as absorber and polystyrene-based scintillating tiles as active material, and is subdivided into one central barrel and two extended barrels. Each barrel is segmented in three layers in depth with a total thickness of 7.4 interaction lengths. The tiles are oriented radially and perpendicular to the beam pipe and grouped in 64 tile modules per barrel, resulting in a near hermetic azimuthal coverage. Wavelength shifting fibres are used to shift the ultraviolet light produced in the scintillator to visible light and guide it into photomultipliers located at the radially far end of each module. The tile calorimeter covers a region with  $|\eta| < 1.7$  and has a granularity of  $\Delta\eta \times \Delta\phi = 0.1 \times 0.1$  except for the outermost layer which has a slightly coarser granularity in  $\eta$ . The design energy resolution of the tile calorimeter is  $\sigma_E/E = 56.4\%/\sqrt{E} \oplus 5.5\%$  [89].

Hadronic calorimetry in the end-caps is provided by two independent calorimeter wheels per end-cap, situated directly behind the electromagnetic end-cap calorimeter (EMEC). Similar to the EMEC, the hadronic end-cap calorimeter (HEC) also uses LAr calorimeter as active material, allowing both calorimeter systems to share a single cryostat per end-cap. Instead of lead, the HEC however uses copper as absorber, which not only drastically reduces the mass of a calorimeter with a given interaction length, but also improves the linearity of low-energy hadronic signals [119]. Each of the four wheels of the HEC is comprised of 32 wedge-shaped modules, divided into two layers in depth. The HEC provides coverage in the region with  $1.5 < |\eta| < 3.2$ , slightly overlapping with the tile calorimeter and thus reducing the drop in material density in the transition region. While the granularity in the precision region with  $1.5 < |\eta| < 2.5$  is the same as for the tile calorimeter, more forward regions with large  $|\eta|$  have a granularity of  $\Delta\eta \times \Delta\phi = 0.2 \times 0.2$  [89]. The design resolution of the HEC is  $\sigma_E/E = 70.6\%/\sqrt{E} \oplus 5.8\%$  [89].

The forward region with  $3.1 < |\eta| < 4.9$  is covered by the LAr forward calorimeter (FCal), which is integrated into the end-cap cryostats. This hermetic design not only minimises energy

losses in cracks between the calorimeter systems, but also reduces the amount of background reaching the muon system in the outer shell of the ATLAS experiment. In order to limit the amount of neutrons reflected into the ID, the FCal is recessed by about 1.2 m with respect to the EM calorimeter, motivating a high-density design due to space constraints. The FCal in each end-cap consists of three layers with a total depth of 10 interaction lengths. While the first layer uses copper as absorber and is optimised for electromagnetic measurements, the remaining two layers are made of tungsten and cover hadronic interactions. The metals comprising each layer are arranged in a matrix structure with electrodes consisting of rods and tubes parallel to the beam pipe filling out regular channels. The small gaps (0.25 mm in the first layer) between the rods and tubes of the electrodes are filled with LAr as active material.

### 2.2.5 Muon spectrometer

Muons, being minimum ionising particles, are the only charged particles that consistently pass through the entire detector including the calorimeter system. Providing one of the cleanest signatures for BSM physics [1], muonic final states are measured with a dedicated detector system on the outermost layer of the ATLAS experiment. Embedded in the magnetic field of the toroid magnets, the muon spectrometer (MS) consists of three concentric cylindrical layers in the barrel region, and three wheels in each end-cap, and provides momentum measurements up to  $|\eta| < 2.7$  [89]. It is designed to deliver a transverse momentum resolution of 10% for 1 TeV tracks and be able to measure muon momenta down to roughly 3 GeV.

The MS uses two high-precision gaseous detector chamber types, Monitoring Drift Tube (MDT) chambers and Cathode Strip Chamber (CSC). As both the MDT and CSC are drift chambers relying on charges drifting to an anode or cathode, the maximum response times of 700 ns and 50 ns, respectively, are slow compared to the bunch-spacing of 25 ns. ATLAS therefore uses Resistive Plate Chamber (RPC) in the barrel and Thin Gap Chamber (TGC) in the end-caps as triggers in order to associate measurements to the right bunch-crossing.

#### Monitored drift tubes

The MDT chambers are the main subcomponent providing precision measurements of the muon tracks up to  $|\eta| < 2.7$ , except in the innermost end-cap layer where their coverage only extends to  $|\eta| < 2.0$ . The MDT are made of 3–4 layers of  $\sim 30$  mm diameter drift tubes operated with Ar/CO<sub>2</sub> gas<sup>†</sup> pressurised to 3 bar. Charged particles traversing the drift tubes ionise the gas, creating electrons that drift towards a central tungsten-rhenium anode wire with a diameter of 50  $\mu\text{m}$ . Following the symmetry of the barrel toroid magnet, the MDT chambers are arranged as octets around the calorimeters with the drift tubes in  $\phi$  direction, i.e. tangential to circles around the beam pipe. In order to be able to correct for potential chamber deformations due to varying thermal gradients, each MDT chamber is equipped with an internal optical alignment system. Apart from the regular chambers in the barrel and the end-cap wheels, special modules are installed in order to minimise the acceptance losses due to the ATLAS support structure (the *feet* of the experiment).

<sup>†</sup> With a small admixture of 300 ppm of water to improve high voltage stability.

## Cathode strip chambers

In the region with  $|\eta| > 2.0$  in the first layer of the end-caps, the particle flux is too high to allow for safe operation of MDT chambers. Instead, CSC, multiwire proportional chambers, are used for precision measurements in this region. The gold-plated tungsten-rhenium anode wires in the CSC have a diameter of  $30\text{ }\mu\text{m}$  and are oriented in radial direction. The wires are enclosed on both sides by cathode planes, one segmented perpendicular to the wires (thus providing the precision coordinate), the other parallel to the wires. Each chamber is filled with an Ar/CO<sub>2</sub> gas mixture and consists of four wire planes, resulting in four measurements of  $\eta$  and  $\phi$  for each track. In addition to the chamber-internal alignment sensors, ATLAS also employs an optical alignment system in order to align the precision chambers to each other [89].

## Resistive plate chambers

RPC are gaseous parallel electrode-plate chambers that use two resistive plastic laminate plates kept 2 mm apart by insulating spacers. Due to an electric field of roughly  $4.9\text{ kV mm}^{-1}$  between the plates, charged particles traversing the chamber cause avalanches of charges that can be read out through capacitive coupling to metallic strips mounted on the outside of the resistive plates. In order to provide tracking information in both coordinates, each RPC consists of two rectangular units each containing two gas volumes with a total of four pairwise orthogonal sets of readout strips. The three concentric cylindrical layers of RPC in the barrel region thus provide six measurements of  $\eta$  and  $\phi$  and cover  $|\eta| < 1.05$

## Thin gap chambers

The TGC are not only necessary for triggering in the end-cap MS but also provide measurements of a second coordinate, orthogonal to the measurements of the MDT. TGC are multi-wire proportional chambers enclosed by two cathode planes and a wire-to-wire gap of 1.8 mm. The gas mixture of CO<sub>2</sub> and n-pentane allows for a quasi-saturated operation mode resulting in a relatively low gas gain. Each TGC unit is built from a doublet or triplet of such chambers, separated by a supporting honeycomb structure. In each unit, the azimuthal coordinate is measured by radial copper readout strips, while the bending coordinate is provided by the wire groups. The TGC are mounted in two concentric disks in each end-cap, one covering the rapidity range  $1.05 < |\eta| < 1.92$  and one covering the more forward region  $1.92 < |\eta| < 2.4$ .

### 2.2.6 Forward detectors

Apart from the relative luminosity monitor LUCID-2 [101] (introduced in section 2.1.2) located at  $\pm 17\text{ m}$  from the IP, ATLAS uses three additional small detectors in the forward region. At  $\pm 140\text{ m}$  from the IP, immediately behind the location where the straight beam pipe splits back into two separate beam pipes, lies the Zero-Degree Calorimeter (ZDC) [120]. The ZDC is embedded in an absorber for neutrals mainly measures forward neutrons with  $|\eta| > 8.3$  in heavy-ion collisions. Even further out from the IP at  $\pm 240\text{ m}$ , lies the Absolute Luminosity for ATLAS (ALFA) detector [121], consisting of scintillating fibre trackers placed in Roman pots [122] measuring the absolute luminosity through small scattering angles of  $3\text{ }\mu\text{rad}$  (necessitating

the special beam conditions also used for the LUCID-2 calibrations). The last of the forward detectors is the ATLAS Forward Proton (AFP) [123] detector, installed at the end of 2016 and operational since early 2017, is situated  $\pm 205$  m and  $\pm 217$  m from the IP and consists of Roman pots containing silicon trackers and time-of-flight detectors. The AFP detectors aims to study very forward protons from elastic and diffractive scattering.

### 2.2.7 Trigger and data acquisition system

With a nominal bunch spacing of 25 ns, the bunch crossing rate within ATLAS is 40 MHz. Even with only a single  $pp$  collision event per bunch crossing, a mean event size of  $\sim 1.6$  MB results in a data volume of more than  $60 \text{ TB s}^{-1}$ , which is impossible to process and write to disk with current technology. In addition, interesting physics events will often only occur at relatively low rates, and generally be hidden in vast amounts of QCD processes that have much higher cross-sections. In order to reduce the event rate written to disk and focus on interesting signatures worth studying, ATLAS used a two-level trigger system during the Run 2 data-taking period [124].

The Level 1 (L1) trigger [125] is hardware-based and uses only coarse granularity calorimeter and muon detector information as inputs in order to define Regions of Interest (ROIs), i.e. regions in  $\eta$  and  $\phi$  with interesting features. With a decision time of only 2.5  $\mu\text{s}$  per event, the L1 trigger reduces the event rate from the bunch-crossing rate of 40 MHz to 100 kHz. The ROIs generated by the L1 trigger are subsequently processed by the High Level Trigger (HLT) [126], a software-based trigger running on a computing farm. The HLT has access to the full detector granularity in the ROIs as well as the entire event and runs reconstruction algorithms similar to those used in offline analysis, allowing to significantly refine the decisions from the L1 trigger. The HLT reduces the event rate from 100 kHz to 1 kHz, matching the data storage constraints. Data flow from the detectors to the storage elements and between the L1 and HLT trigger elements is handled by the Data Acquisition System (DAQ) [126].

### 2.2.8 Monte Carlo simulation

Monte Carlo (MC) methods play a crucial role for simulating physics events in ATLAS. MC simulations are computational algorithms using repeated random sampling to solve complex problems, often the estimation of multi-dimensional integrals for which analytical solutions are not known. According to the law of large numbers the numerical approximations obtained by such a stochastic method become more accurate, the larger the sample size is. In addition, the central limit theorem also allows to state an uncertainty on the estimation of an expected value. This method can in principle be used for any problem with a probabilistic interpretation is this true?

In the ATLAS experiment, MC methods are not only used in physics analysis to estimate contributions from various physics processes in different phase space regions, but also to simulate particle interactions with the detector material and even finds ample applications in detector design and optimisation as well as physics objects reconstruction techniques. All of these applications rely on the MC simulations being as precise as possible, i.e. correctly describing the physics processes and detector responses underlying the data recorded by the ATLAS

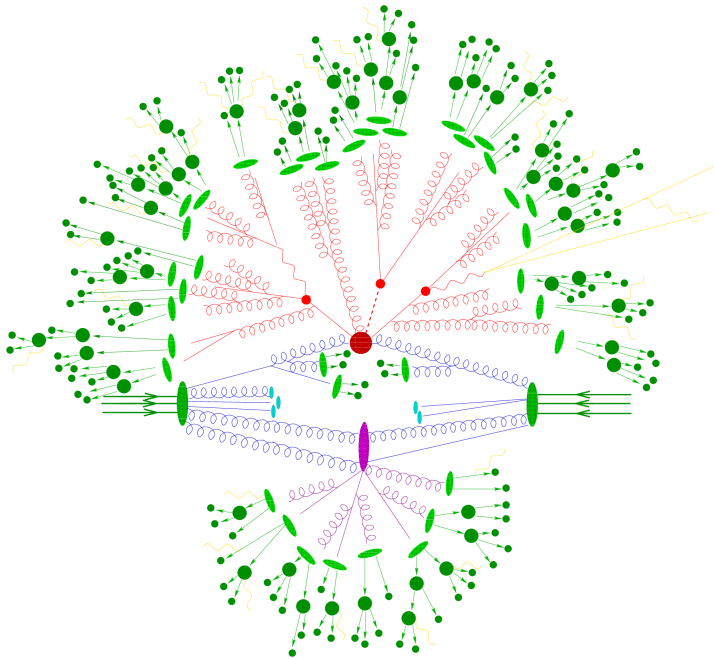


**Figure 2.7:** Pictorial representation of a  $t\bar{t} + H$  event simulated by a MC event generator. The hard interaction (big red blob) is followed by the decay of the two top quarks and the Higgs boson (small red blobs). ISR and FSR are shown as curly blue and red lines, respectively. A second interaction is simulated (purple blob) and contributions from the underlying event are modelled (purple lines). The hadronisation of final-state partons (light green blobs) is followed by the decays of unstable hadrons (dark green blobs). QED radiation (yellow lines) is added at each stage of the event simulation. Figure adapted from [128].

experiment. For reasons of more efficient computing resource utilisation and easier software validation, the ATLAS simulation infrastructure [127] can be divided into three main steps:

- (i) Event generation,
- (ii) Detector simulation,
- (iii) Digitisation,

producing an output format identical to that of the DAQ for recorded  $pp$  collision events, such that the same trigger and reconstruction algorithms can be run over simulated data.

### Event generation

The majority of  $pp$  collisions are not interesting for particle physicists in the sense that they only involve soft hadrons travelling along the beam axis. Only a few events actually involve an *hard-scattering* event with high-momentum transfer, rendering them interesting for particle physicists to study. Generating and understanding the final states of these  $pp$  collision events is an enormously challenging problem as it typically involves hundreds of particles with energies spanning many orders of magnitude [129]. This makes the matrix elements connected to these processes too complicated to be computed beyond the first few orders of perturbation theory. The treatment of divergences and the integration over large phase-spaces further complicates the calculation of experimental observables.

It is not surprising that the simulation of the hard-scatter interaction is at the heart of any MC event generator. Due to the high-momentum transfer scale, the cross section of this process can

simulation tools allow to plugin any Lagrangian and get events at detector level

be calculated perturbatively using collinear factorisation [129],

$$\sigma = \sum_{a,b} \int_0^1 dx_a dx_b \int d\Phi_n f_a^{h_1}(x_a, \mu_F) f_b^{h_2}(x_b, \mu_F) \times \frac{1}{2x_a x_b s} |\mathcal{M}_{ab \rightarrow n}|^2(\Phi_n; \mu_F, \mu_R), \quad (2.7)$$

with  $x_a$  and  $x_b$  the momentum fractions of the partons  $a$  and  $b$  with respect to their parent hadrons  $h_1$  and  $h_2$ ,  $\mu_F$  and  $\mu_R$  are the unphysical factorisation and the renormalisation scales, respectively and  $d\Phi_n$  is the differential final state phase-space element. The phase space integration is typically done using MC sampling methods. The choices for  $\mu_R$  and  $\mu_F$  are to some degree arbitrary, but are typically chosen to be in accordance with the logarithmic structure of quantum chromodynamics (QCD), such that the matrix elements can be combined with the subsequent parton showers [129]. The Matrix Element (ME)  $|\mathcal{M}_{ab \rightarrow n}|^2$  can be calculated using different methods [129], with most MC generators employing leading order (LO) computations. As LO matrix elements are only reliable for the shapes of the distributions, an additional  $K$ -factor correcting the normalisation of the cross section to next-to-leading order (NLO) is typically used. The probability of finding a parton with momentum fractions  $x$  in a hadron  $h$ , is given by the PDF  $f_a^h(x, \mu_F)$  and depends on the probed factorisation scale  $\mu_F$ . The PDFs depend on non-perturbative aspects of the proton wave function and can thus not be calculated from first principles. Instead, they are extracted from measurements in deep inelastic scattering experiments (see e.g. [130, 131]). The variety of PDFs provided by different groups, is accessible in a common format through a unified interface implemented by the LHAPDF library [132]. In MC generators, the choice of PDFs not only play a crucial role for the simulation of the hard process, but also in the subsequent parton showers and multiple parton interactions, thus influencing both cross sections and event shapes.

Fixed-order matrix elements work well for describing separated, hard partons but is not sufficient to describe soft and collinear partons. Higher order effects from gluon radiation can be simulated using a Parton Shower (PS) algorithm. The emitted gluons will radiate additional gluons or split into quark–antiquark pairs which can in turn undergo gluon radiation. The PS thus describes an evolutionary process in momentum transfer scales from the scale of the hard scatter interaction down to the infrared scale  $\mathcal{O}(1 \text{ GeV})$  where QCD becomes non-perturbative and partons are confined into hadrons. Both ISR and FSR are simulated through the PS. As opposed to ME calculations, PSs offer poor modelling of few hard partons, but excel in the simulation of collinear and soft multi-parton states.

In order to avoid double counting, the hard partons described by the calculation of the ME and the soft collinear emissions of the PS have to be connected to each other. This is done either through *matching* or *merging*. ME matching approaches [133] integrate higher-order corrections to an inclusive process with the PS [129]. Merging techniques like the CKKW [134] or CKKW-L [135] methods define an unphysical merging scale which can be understood as a jet resolution scale such that higher order ME corrections are only calculated for jets above that scale (while jets below that scale are modelled with the PS).

Next, additional activity in the event not directly associated to the hard process is simulated. The underlying event is typically defined to be all additional activity after ISR and FSR off the hard process has been taken into account [129]. Furthermore, *multiple interactions* can occur in a single  $pp$  collision. The modelling of multiple interactions involves multiple hard scatter

processes per  $pp$  collision as well as multiple soft interactions in addition to the hard scatter process.

Once the PS reaches energies of  $\mathcal{O}(1 \text{ GeV})$ , entering the non-perturbative regime of QCD, the coloured objects need to be transformed into colourless states. This so-called *hadronisation* step cannot be calculated from first principles but has to be modelled, typically with either a *string* or a *cluster* model. The most advanced of the string models is the *Lund* model [136, 137]. It starts from linear confinement and considers a linear potential between a  $q\bar{q}$  pair, that can be thought of as a uniform colour flux tube stretching between the  $q$  and  $\bar{q}$ , with a transverse dimension of the order of typical hadronic size (i.e. around 1 fm). As the  $q\bar{q}$  pair moves apart, the flux tube stretches in length, leading to an increase in potential energy, finally breaking apart once enough energy is available to create a new  $q'\bar{q}'$  pair, resulting in two colourless quark pairs  $q\bar{q}'$  and  $q'\bar{q}$ . The new quark pairs can again move apart and break up further, leading to quark anti-quark pairs with low relative momentum, forming the final hadrons. The cluster model is based on the preconfinement property of PSs [138], stating that the colourless clusters of partons can be formed at any evolution scale  $Q_0$  of the PS, and result in universal invariant mass distributions that depend only on  $Q_0$  and the QCD scale  $\Lambda$ , but not on the energy scale  $Q$  or nature of the hard process at the origin of the PS [129]. The universal invariant mass distribution holds in the asymptotic limit where  $Q_0 \ll Q$ . If further  $Q_0 \gg \Lambda$ , then the mass, momentum and multiplicity distributions of the colourless clusters can even be calculated perturbatively [129]. Cluster models start with non-perturbative splitting of gluons and  $q\bar{q}$  pairs, followed by the formation of clusters from colour-connected pairs. Clusters further split up until the  $Q_0$  scale is reached, where they form the final mesons.

As not all hadrons formed in the hadronisation process are stable, the affected hadrons need to be decayed until they form resonances stable enough to reach the detector material. In addition QED radiation, that can happen at any time during the event, needs to be simulated. This is typically done with algorithms similar to the ones used for the PS.

The simulation steps that cannot be performed from first principles but rely on phenomenological models (underlying event, PS, hadronisation) introduce free parameters that need to be derived or *tuned* from parameter optimisations against experimental data. In ATLAS, the output of MC event generators is stored in so-called EVNT data format containing HepMC [139] event records. Although only the stable final-state particles are propagated to the detector simulation, the HepMC event record contains the entire connected tree as so-called *Monte Carlo truth*.

## Detector simulation

Only the final-state particles generated by the MC event generator are read into the detector simulation. In ATLAS, the full detector simulation is handled GEANT4 [140], a toolkit providing detailed models for physics processes and an infrastructure for particle transportation through a geometry. GEANT4 has knowledge about the full detector geometry as well as the materials used in the subdetectors and is able to compute the energy deposits (so-called *hits*) from single particles in the different sensitive portions of the detector components. The GEANT4 simulation adds information to the Monte Carlo truth content created during the event generation, including however only the most relevant tracks (mostly from the ID) due to size constraints [127].

The complicated detector geometry and the detailed description of physics processes requires large computing resources for the full detector simulation using GEANT4, rendering it inaccessible for many physics studies requiring large statistics. Several varieties of fast simulations are available to this end. One of the most-used ones is ATLFAST-II [127], a fast simulation that uses the GEANT4 full simulation only for the ID and MS. The slow simulation in the calorimeters—that takes about 80% of the full simulation time—is replaced with FASTCALOSIM [141], using parameterised electromagnetic and hadronic showers. Compared to the  $\mathcal{O}(10^3)$  s simulation time per event in the full simulation, the ATLFAST-II detector simulation only takes  $\mathcal{O}(10^2)$  s [127].

## Digitisation

During the digitisation step, the hits from the detector simulation are converted into detector responses, so-called *digits* that are typically produced when currents or voltages in the respective readout channels rise above a certain threshold in a given time window. The digitisation considers a modelling of the peculiarities of each detector component, including electronic noise and cross-talk [127]. The effects from out-of-time and in-time pile-up are also considered by reading in multiple events and overlaying their hits. In order to match the true pile-up distribution in data, the number of events to overlay per bunch crossing can be set at run time. As described in section 2.1.1, effects from cavern background, beam halo and beam gas can either be mitigated or removed at analysis level and are therefore typically not simulated.

MCViz signal event?

## **Part II**

# **The 1-lepton analysis**





# **Part III**

# **Reinterpretation**





## **Part IV**

# **Summary and Outlook**





# **Part V**

# **Appendix**



# Abbreviations

**AFP** ATLAS Forward Proton. [51](#)

**ALFA** Absolute Luminosity for ATLAS. [50](#)

**BSM** beyond the Standard Model. [41](#), [43](#), [49](#)

**CSC** Cathode Strip Chamber. [49](#), [50](#)

**DAQ** Data Acquisition System. [51](#), [52](#)

**EM** Electromagnetic. [48](#), [49](#)

**EMEC** electromagnetic end-cap calorimeter. [48](#)

**FCal** forward calorimeter. [48](#), [49](#)

**FSR** Final State Radiation. [52](#), [53](#)

**HEC** hadronic end-cap calorimeter. [48](#)

**HLT** High Level Trigger. [51](#)

**IBL** insertable B-layer. [45](#)

**ID** inner detector. [45–47](#), [49](#), [54](#), [55](#)

**IP** interaction point. [43–45](#), [50](#), [51](#)

**ISR** Initial State Radiation. [52](#), [53](#)

**L1** Level 1. [51](#)

**LAr** liquid argon. [48](#), [49](#)

**LEP** Large Electron Positron. [37](#)

**LHC** Large Hadron Collider. [37–39](#), [41–44](#)

**LO** leading order. [53](#)

- MC** Monte Carlo. 51–54
- MDT** Monitoring Drift Tube. 49, 50
- ME** Matrix Element. 53
- MS** muon spectrometer. 49, 50, 55
- NLO** next-to-leading order. 53
- PDF** Parton Distribution Function. 44, 53
- pdf** Probability Density Function. 51
- PS** Parton Shower. 53, 54
- QCD** quantum chromodynamics. 53, 54
- QED** quantum electrodynamics. 52, 54
- RF** radio frequency. 38, 39
- ROIs** Regions of Interest. 51
- RPC** Resistive Plate Chamber. 49, 50
- SCT** silicon microstrip tracker. 45, 46
- SUSY** Supersymmetry. 37, 41
- TGC** Thin Gap Chamber. 49, 50
- TRT** transition radiation tracker. 45–47
- vdM** van der Meer. 42
- ZDC** Zero-Degree Calorimeter. 50

# Bibliography

- [1] I. C. Brock and T. Schorner-Sadenius, *Physics at the terascale*. Wiley, Weinheim, 2011. <https://cds.cern.ch/record/1354959>.
- [2] M. E. Peskin and D. V. Schroeder, *An Introduction to quantum field theory*. Addison-Wesley, Reading, USA, 1995. <http://www.slac.stanford.edu/~mpeskin/QFT.html>.
- [3] S. P. Martin, “A Supersymmetry primer,” [arXiv:hep-ph/9709356 \[hep-ph\]](https://arxiv.org/abs/hep-ph/9709356). [Adv. Ser. Direct. High Energy Phys.18,1(1998)].
- [4] M. Bustamante, L. Cieri, and J. Ellis, “Beyond the Standard Model for Montaneros,” in *5th CERN - Latin American School of High-Energy Physics*. 11, 2009. [arXiv:0911.4409 \[hep-ph\]](https://arxiv.org/abs/0911.4409).
- [5] L. Brown, *The Birth of particle physics*. Cambridge University Press, Cambridge Cambridgeshire New York, 1986.
- [6] P. J. Mohr, D. B. Newell, and B. N. Taylor, “CODATA Recommended Values of the Fundamental Physical Constants: 2014,” *Rev. Mod. Phys.* **88** no. 3, (2016) 035009, [arXiv:1507.07956 \[physics.atom-ph\]](https://arxiv.org/abs/1507.07956).
- [7] P. D. Group, “Review of Particle Physics,” *Progress of Theoretical and Experimental Physics* **2020** no. 8, (08, 2020), <https://academic.oup.com/ptep/article-pdf/2020/8/083C01/34673722/ptaa104.pdf>. <https://doi.org/10.1093/ptep/ptaa104>. 083C01.
- [8] **Super-Kamiokande** Collaboration, Y. Fukuda *et al.*, “Evidence for oscillation of atmospheric neutrinos,” *Phys. Rev. Lett.* **81** (1998) 1562–1567, [arXiv:hep-ex/9807003 \[hep-ex\]](https://arxiv.org/abs/hep-ex/9807003).
- [9] Z. Maki, M. Nakagawa, and S. Sakata, “Remarks on the unified model of elementary particles,” *Prog. Theor. Phys.* **28** (1962) 870–880. [,34(1962)].
- [10] N. Cabibbo, “Unitary symmetry and leptonic decays,” *Phys. Rev. Lett.* **10** (Jun, 1963) 531–533. <https://link.aps.org/doi/10.1103/PhysRevLett.10.531>.
- [11] M. Kobayashi and T. Maskawa, “CP Violation in the Renormalizable Theory of Weak Interaction,” *Prog. Theor. Phys.* **49** (1973) 652–657.
- [12] E. Noether and M. A. Tavel, “Invariant variation problems,” [arXiv:physics/0503066](https://arxiv.org/abs/physics/0503066).
- [13] J. C. Ward, “An identity in quantum electrodynamics,” *Phys. Rev.* **78** (Apr, 1950) 182–182. <https://link.aps.org/doi/10.1103/PhysRev.78.182>.

- [14] Y. Takahashi, “On the generalized ward identity,” *Il Nuovo Cimento (1955-1965)* **6** no. 2, (Aug, 1957) 371–375. <https://doi.org/10.1007/BF02832514>.
- [15] G. ’tHooft, “Renormalization of massless yang-mills fields,” *Nuclear Physics B* **33** no. 1, (1971) 173 – 199. <http://www.sciencedirect.com/science/article/pii/0550321371903956>.
- [16] J. Taylor, “Ward identities and charge renormalization of the yang-mills field,” *Nuclear Physics B* **33** no. 2, (1971) 436 – 444. <http://www.sciencedirect.com/science/article/pii/0550321371902975>.
- [17] A. A. Slavnov, “Ward identities in gauge theories,” *Theoretical and Mathematical Physics* **10** no. 2, (Feb, 1972) 99–104. <https://doi.org/10.1007/BF01090719>.
- [18] C. N. Yang and R. L. Mills, “Conservation of isotopic spin and isotopic gauge invariance,” *Phys. Rev.* **96** (Oct, 1954) 191–195. <https://link.aps.org/doi/10.1103/PhysRev.96.191>.
- [19] K. G. Wilson, “Confinement of quarks,” *Phys. Rev. D* **10** (Oct, 1974) 2445–2459. <https://link.aps.org/doi/10.1103/PhysRevD.10.2445>.
- [20] T. DeGrand and C. DeTar, *Lattice Methods for Quantum Chromodynamics*. World Scientific, Singapore, 2006. <https://cds.cern.ch/record/1055545>.
- [21] S. L. Glashow, “Partial-symmetries of weak interactions,” *Nuclear Physics* **22** no. 4, (1961) 579 – 588. <http://www.sciencedirect.com/science/article/pii/0029558261904692>.
- [22] S. Weinberg, “A model of leptons,” *Phys. Rev. Lett.* **19** (Nov, 1967) 1264–1266. <https://link.aps.org/doi/10.1103/PhysRevLett.19.1264>.
- [23] A. Salam and J. C. Ward, “Weak and electromagnetic interactions,” *Il Nuovo Cimento (1955-1965)* **11** no. 4, (Feb, 1959) 568–577. <https://doi.org/10.1007/BF02726525>.
- [24] C. S. Wu, E. Ambler, R. W. Hayward, D. D. Hoppes, and R. P. Hudson, “Experimental test of parity conservation in beta decay,” *Phys. Rev.* **105** (Feb, 1957) 1413–1415. <https://link.aps.org/doi/10.1103/PhysRev.105.1413>.
- [25] M. Gell-Mann, “The interpretation of the new particles as displaced charge multiplets,” *Il Nuovo Cimento (1955-1965)* **4** no. 2, (Apr, 1956) 848–866. <https://doi.org/10.1007/BF02748000>.
- [26] K. Nishijima, “Charge Independence Theory of V Particles\*,” *Progress of Theoretical Physics* **13** no. 3, (03, 1955) 285–304, <https://academic.oup.com/ptp/article-pdf/13/3/285/5425869/13-3-285.pdf>. <https://doi.org/10.1143/PTP.13.285>.
- [27] T. Nakano and K. Nishijima, “Charge Independence for V-particles\*,” *Progress of Theoretical Physics* **10** no. 5, (11, 1953) 581–582, <https://academic.oup.com/ptp/article-pdf/10/5/581/5364926/10-5-581.pdf>. <https://doi.org/10.1143/PTP.10.581>.
- [28] F. Englert and R. Brout, “Broken symmetry and the mass of gauge vector mesons,” *Phys. Rev. Lett.* **13** (Aug, 1964) 321–323. <https://link.aps.org/doi/10.1103/PhysRevLett.13.321>.
- [29] P. W. Higgs, “Broken symmetries and the masses of gauge bosons,” *Phys. Rev. Lett.* **13** (Oct, 1964) 508–509. <https://link.aps.org/doi/10.1103/PhysRevLett.13.508>.

- [30] P. W. Higgs, “Spontaneous symmetry breakdown without massless bosons,” *Phys. Rev.* **145** (May, 1966) 1156–1163. <https://link.aps.org/doi/10.1103/PhysRev.145.1156>.
- [31] Y. Nambu, “Quasiparticles and Gauge Invariance in the Theory of Superconductivity,” *Phys. Rev.* **117** (1960) 648–663. [[132\(1960\)](#)].
- [32] J. Goldstone, “Field Theories with Superconductor Solutions,” *Nuovo Cim.* **19** (1961) 154–164.
- [33] V. Brdar, A. J. Helmboldt, S. Iwamoto, and K. Schmitz, “Type-I Seesaw as the Common Origin of Neutrino Mass, Baryon Asymmetry, and the Electroweak Scale,” *Phys. Rev. D* **100** (2019) 075029, [arXiv:1905.12634 \[hep-ph\]](https://arxiv.org/abs/1905.12634).
- [34] G. ’t Hooft and M. Veltman, “Regularization and renormalization of gauge fields,” *Nuclear Physics B* **44** no. 1, (1972) 189 – 213. <http://www.sciencedirect.com/science/article/pii/0550321372902799>.
- [35] F. Zwicky, “Die Rotverschiebung von extragalaktischen Nebeln,” *Helv. Phys. Acta* **6** (1933) 110–127. <https://cds.cern.ch/record/437297>.
- [36] V. C. Rubin and W. K. Ford, Jr., “Rotation of the Andromeda Nebula from a Spectroscopic Survey of Emission Regions,” *Astrophys. J.* **159** (1970) 379–403.
- [37] G. Bertone, D. Hooper, and J. Silk, “Particle dark matter: Evidence, candidates and constraints,” *Phys. Rept.* **405** (2005) 279–390, [arXiv:hep-ph/0404175](https://arxiv.org/abs/hep-ph/0404175).
- [38] D. Clowe, M. Bradac, A. H. Gonzalez, M. Markevitch, S. W. Randall, C. Jones, and D. Zaritsky, “A direct empirical proof of the existence of dark matter,” *Astrophys. J.* **648** (2006) L109–L113, [arXiv:astro-ph/0608407 \[astro-ph\]](https://arxiv.org/abs/astro-ph/0608407).
- [39] A. Taylor, S. Dye, T. J. Broadhurst, N. Benitez, and E. van Kampen, “Gravitational lens magnification and the mass of abell 1689,” *Astrophys. J.* **501** (1998) 539, [arXiv:astro-ph/9801158](https://arxiv.org/abs/astro-ph/9801158).
- [40] C. Bennett *et al.*, “Four year COBE DMR cosmic microwave background observations: Maps and basic results,” *Astrophys. J. Lett.* **464** (1996) L1–L4, [arXiv:astro-ph/9601067](https://arxiv.org/abs/astro-ph/9601067).
- [41] G. F. Smoot *et al.*, “Structure in the COBE Differential Microwave Radiometer First-Year Maps,” *ApJS* **396** (September, 1992) L1.
- [42] **WMAP** Collaboration, “Nine-year Wilkinson Microwave Anisotropy Probe (WMAP) Observations: Final Maps and Results,” *ApJS* **208** no. 2, (October, 2013) 20, [arXiv:1212.5225 \[astro-ph.CO\]](https://arxiv.org/abs/1212.5225).
- [43] **WMAP** Collaboration, “Nine-year Wilkinson Microwave Anisotropy Probe (WMAP) Observations: Cosmological Parameter Results,” *ApJS* **208** no. 2, (October, 2013) 19, [arXiv:1212.5226 \[astro-ph.CO\]](https://arxiv.org/abs/1212.5226).
- [44] **Planck** Collaboration, “Planck 2018 results. I. Overview and the cosmological legacy of Planck,” *Astron. Astrophys.* **641** (2020) A1, [arXiv:1807.06205 \[astro-ph.CO\]](https://arxiv.org/abs/1807.06205).
- [45] A. Liddle, *An introduction to modern cosmology; 3rd ed.* Wiley, Chichester, Mar, 2015. <https://cds.cern.ch/record/1976476>.
- [46] **Planck** Collaboration, “Planck 2018 results. VI. Cosmological parameters,” *Astron. Astrophys.* **641** (2020) A6, [arXiv:1807.06209 \[astro-ph.CO\]](https://arxiv.org/abs/1807.06209).

- [47] H. Georgi and S. L. Glashow, “Unity of all elementary-particle forces,” *Phys. Rev. Lett.* **32** (Feb, 1974) 438–441. <https://link.aps.org/doi/10.1103/PhysRevLett.32.438>.
- [48] I. Aitchison, *Supersymmetry in Particle Physics. An Elementary Introduction*. Cambridge University Press, Cambridge, 2007.
- [49] **Muon g-2** Collaboration, G. Bennett *et al.*, “Final Report of the Muon E821 Anomalous Magnetic Moment Measurement at BNL,” *Phys. Rev. D* **73** (2006) 072003, [arXiv:hep-ex/0602035](https://arxiv.org/abs/hep-ex/0602035).
- [50] H. Baer and X. Tata, *Weak Scale Supersymmetry: From Superfields to Scattering Events*. Cambridge University Press, 2006.
- [51] A. Czarnecki and W. J. Marciano, “The Muon anomalous magnetic moment: A Harbinger for ‘new physics’,” *Phys. Rev. D* **64** (2001) 013014, [arXiv:hep-ph/0102122](https://arxiv.org/abs/hep-ph/0102122).
- [52] J. L. Feng and K. T. Matchev, “Supersymmetry and the anomalous magnetic moment of the muon,” *Phys. Rev. Lett.* **86** (2001) 3480–3483, [arXiv:hep-ph/0102146](https://arxiv.org/abs/hep-ph/0102146).
- [53] S. Coleman and J. Mandula, “All possible symmetries of the  $s$  matrix,” *Phys. Rev.* **159** (Jul, 1967) 1251–1256. <https://link.aps.org/doi/10.1103/PhysRev.159.1251>.
- [54] R. Haag, J. T. Lopuszanski, and M. Sohnius, “All Possible Generators of Supersymmetries of the  $s$  Matrix,” *Nucl. Phys.* **B88** (1975) 257. [,257(1974)].
- [55] J. Wess and B. Zumino, “Supergauge transformations in four dimensions,” *Nuclear Physics B* **70** no. 1, (1974) 39 – 50.  
<http://www.sciencedirect.com/science/article/pii/0550321374903551>.
- [56] H. Georgi and S. L. Glashow, “Gauge theories without anomalies,” *Phys. Rev. D* **6** (Jul, 1972) 429–431. <https://link.aps.org/doi/10.1103/PhysRevD.6.429>.
- [57] S. Dimopoulos and D. W. Sutter, “The Supersymmetric flavor problem,” *Nucl. Phys. B* **452** (1995) 496–512, [arXiv:hep-ph/9504415](https://arxiv.org/abs/hep-ph/9504415).
- [58] **MEG** Collaboration, T. Mori, “Final Results of the MEG Experiment,” *Nuovo Cim. C* **39** no. 4, (2017) 325, [arXiv:1606.08168 \[hep-ex\]](https://arxiv.org/abs/1606.08168).
- [59] H. P. Nilles, “Supersymmetry, Supergravity and Particle Physics,” *Phys. Rept.* **110** (1984) 1–162.
- [60] A. Lahanas and D. Nanopoulos, “The road to no-scale supergravity,” *Physics Reports* **145** no. 1, (1987) 1 – 139.  
<http://www.sciencedirect.com/science/article/pii/0370157387900342>.
- [61] J. L. Feng, A. Rajaraman, and F. Takayama, “Superweakly interacting massive particles,” *Phys. Rev. Lett.* **91** (2003) 011302, [arXiv:hep-ph/0302215](https://arxiv.org/abs/hep-ph/0302215).
- [62] **Super-Kamiokande** Collaboration, K. Abe *et al.*, “Search for proton decay via  $p \rightarrow e^+ \pi^0$  and  $p \rightarrow \mu^+ \pi^0$  in 0.31 megaton-years exposure of the Super-Kamiokande water Cherenkov detector,” *Phys. Rev. D* **95** no. 1, (2017) 012004, [arXiv:1610.03597 \[hep-ex\]](https://arxiv.org/abs/1610.03597).
- [63] J. R. Ellis, “Beyond the standard model for hill walkers,” in *1998 European School of High-Energy Physics*, pp. 133–196. 8, 1998. [arXiv:hep-ph/9812235](https://arxiv.org/abs/hep-ph/9812235).

- [64] J. R. Ellis, J. Hagelin, D. V. Nanopoulos, K. A. Olive, and M. Srednicki, “Supersymmetric Relics from the Big Bang,” *Nucl. Phys. B* **238** (1984) 453–476.
- [65] D. O. Caldwell, R. M. Eisberg, D. M. Grumm, M. S. Witherell, B. Sadoulet, F. S. Goulding, and A. R. Smith, “Laboratory limits on galactic cold dark matter,” *Phys. Rev. Lett.* **61** (Aug, 1988) 510–513. <https://link.aps.org/doi/10.1103/PhysRevLett.61.510>.
- [66] M. Mori, M. M. Nojiri, K. S. Hirata, K. Kihara, Y. Oyama, A. Suzuki, K. Takahashi, M. Yamada, H. Takei, M. Koga, K. Miyano, H. Miyata, Y. Fukuda, T. Hayakawa, K. Inoue, T. Ishida, T. Kajita, Y. Koshio, M. Nakahata, K. Nakamura, A. Sakai, N. Sato, M. Shiozawa, J. Suzuki, Y. Suzuki, Y. Totsuka, M. Koshiba, K. Nishijima, T. Kajimura, T. Suda, A. T. Suzuki, T. Hara, Y. Nagashima, M. Takita, H. Yokoyama, A. Yoshimoto, K. Kaneyuki, Y. Takeuchi, T. Tanimori, S. Tasaka, and K. Nishikawa, “Search for neutralino dark matter heavier than the  $w$  boson at kamiokande,” *Phys. Rev. D* **48** (Dec, 1993) 5505–5518. <https://link.aps.org/doi/10.1103/PhysRevD.48.5505>.
- [67] **CDMS** Collaboration, D. S. Akerib *et al.*, “Exclusion limits on the WIMP-nucleon cross section from the first run of the Cryogenic Dark Matter Search in the Soudan Underground Laboratory,” *Phys. Rev. D* **72** (2005) 052009, [arXiv:astro-ph/0507190](https://arxiv.org/abs/astro-ph/0507190).
- [68] A. Djouadi, J.-L. Kneur, and G. Moultaka, “SuSpect: A Fortran code for the supersymmetric and Higgs particle spectrum in the MSSM,” *Comput. Phys. Commun.* **176** (2007) 426–455, [arXiv:hep-ph/0211331](https://arxiv.org/abs/hep-ph/0211331).
- [69] C. F. Berger, J. S. Gainer, J. L. Hewett, and T. G. Rizzo, “Supersymmetry without prejudice,” *Journal of High Energy Physics* **2009** no. 02, (Feb, 2009) 023–023. <http://dx.doi.org/10.1088/1126-6708/2009/02/023>.
- [70] J. Alwall, P. Schuster, and N. Toro, “Simplified Models for a First Characterization of New Physics at the LHC,” *Phys. Rev. D* **79** (2009) 075020, [arXiv:0810.3921 \[hep-ph\]](https://arxiv.org/abs/0810.3921).
- [71] **LHC New Physics Working Group** Collaboration, D. Alves, “Simplified Models for LHC New Physics Searches,” *J. Phys. G* **39** (2012) 105005, [arXiv:1105.2838 \[hep-ph\]](https://arxiv.org/abs/1105.2838).
- [72] D. S. Alves, E. Izaguirre, and J. G. Wacker, “Where the Sidewalk Ends: Jets and Missing Energy Search Strategies for the 7 TeV LHC,” *JHEP* **10** (2011) 012, [arXiv:1102.5338 \[hep-ph\]](https://arxiv.org/abs/1102.5338).
- [73] F. Ambrogi, S. Kraml, S. Kulkarni, U. Laa, A. Lessa, and W. Waltenberger, “On the coverage of the pMSSM by simplified model results,” *Eur. Phys. J. C* **78** no. 3, (2018) 215, [arXiv:1707.09036 \[hep-ph\]](https://arxiv.org/abs/1707.09036).
- [74] O. Buchmueller and J. Marrouche, “Universal mass limits on gluino and third-generation squarks in the context of Natural-like SUSY spectra,” *Int. J. Mod. Phys. A* **29** no. 06, (2014) 1450032, [arXiv:1304.2185 \[hep-ph\]](https://arxiv.org/abs/1304.2185).
- [75] **ATLAS** Collaboration, M. Aaboud *et al.*, “Dark matter interpretations of ATLAS searches for the electroweak production of supersymmetric particles in  $\sqrt{s} = 8$  TeV proton-proton collisions,” *JHEP* **09** (2016) 175, [arXiv:1608.00872 \[hep-ex\]](https://arxiv.org/abs/1608.00872).
- [76] **ATLAS** Collaboration, “Summary of the ATLAS experiment’s sensitivity to supersymmetry after LHC Run 1 — interpreted in the phenomenological MSSM,” *JHEP* **10** (2015) 134, [arXiv:1508.06608 \[hep-ex\]](https://arxiv.org/abs/1508.06608).

- [77] **ATLAS** Collaboration, “Mass reach of the atlas searches for supersymmetry.” [https://atlas.web.cern.ch/Atlas/GROUPS/PHYSICS/PUBNOTES/ATL-PHYS-PUB-2020-020/fig\\_23.png](https://atlas.web.cern.ch/Atlas/GROUPS/PHYSICS/PUBNOTES/ATL-PHYS-PUB-2020-020/fig_23.png), 2020.
- [78] **CMS** Collaboration, “Summary plot moriond 2017.” [https://twiki.cern.ch/twiki/pub/CMSPublic/SUSYSummary2017/Moriond2017\\_BarPlot.pdf](https://twiki.cern.ch/twiki/pub/CMSPublic/SUSYSummary2017/Moriond2017_BarPlot.pdf), 2017.
- [79] L. S. W. Group, “Notes lepsusywg/02-04.1 and lepsusywg/01-03.1.” <http://lepsusy.web.cern.ch/lepsusy/>, 2004. Accessed: 2021-02-11.
- [80] **ATLAS** Collaboration, G. Aad *et al.*, “Observation of a new particle in the search for the Standard Model Higgs boson with the ATLAS detector at the LHC,” *Phys. Lett. B* **716** (2012) 1–29, [arXiv:1207.7214 \[hep-ex\]](https://arxiv.org/abs/1207.7214).
- [81] **CMS** Collaboration, S. Chatrchyan *et al.*, “Observation of a New Boson at a Mass of 125 GeV with the CMS Experiment at the LHC,” *Phys. Lett. B* **716** (2012) 30–61, [arXiv:1207.7235 \[hep-ex\]](https://arxiv.org/abs/1207.7235).
- [82] CERN, “About cern.” <https://home.cern/about>. Accessed: 2021-01-21.
- [83] CERN, “CERN Annual report 2019,” tech. rep., CERN, Geneva, 2020. <https://cds.cern.ch/record/2723123>.
- [84] O. S. Bruning, P. Collier, P. Lebrun, S. Myers, R. Ostojic, J. Poole, and P. Proudlock, *LHC Design Report*. CERN Yellow Reports: Monographs. CERN, Geneva, 2004. <https://cds.cern.ch/record/782076>.
- [85] M. Blewett and N. Vogt-Nilsen, “Proceedings of the 8th international conference on high-energy accelerators, cern 1971. conference held at geneva, 20–24 september 1971.,” tech. rep., 1971, 1971.
- [86] L. R. Evans and P. Bryant, “LHC Machine,” *JINST* **3** (2008) S08001. 164 p. [http://cds.cern.ch/record/1129806](https://cds.cern.ch/record/1129806). This report is an abridged version of the LHC Design Report (CERN-2004-003).
- [87] R. Scrivens, M. Kronberger, D. Küchler, J. Lettry, C. Mastrostefano, O. Midttun, M. O’Neil, H. Pereira, and C. Schmitzer, “Overview of the status and developments on primary ion sources at CERN\*.” <https://cds.cern.ch/record/1382102>.
- [88] E. Mobs, “The CERN accelerator complex - 2019. Complexe des accélérateurs du CERN - 2019.” <https://cds.cern.ch/record/2684277>. General Photo.
- [89] **ATLAS** Collaboration, “The ATLAS Experiment at the CERN Large Hadron Collider,” *JINST* **3** (2008) S08003.
- [90] **CMS** Collaboration, S. Chatrchyan *et al.*, “The CMS Experiment at the CERN LHC,” *JINST* **3** (2008) S08004.
- [91] **ALICE** Collaboration, K. Aamodt *et al.*, “The ALICE experiment at the CERN LHC,” *JINST* **3** (2008) S08002.
- [92] **LHCb** Collaboration, J. Alves, A. Augusto *et al.*, “The LHCb Detector at the LHC,” *JINST* **3** (2008) S08005.
- [93] **TOTEM** Collaboration, G. Anelli *et al.*, “The TOTEM experiment at the CERN Large Hadron Collider,” *JINST* **3** (2008) S08007.

- [94] **LHCf** Collaboration, O. Adriani *et al.*, “Technical design report of the LHCf experiment: Measurement of photons and neutral pions in the very forward region of LHC,”.
- [95] **MoEDAL** Collaboration, J. Pinfold *et al.*, “Technical Design Report of the MoEDAL Experiment,”.
- [96] **ATLAS** Collaboration, “ATLAS Public Results - Luminosity Public Results Run 2.”, <https://twiki.cern.ch/twiki/bin/view/AtlasPublic/LuminosityPublicResultsRun2>. Accessed: 2021-01-17.
- [97] **ATLAS** Collaboration, Z. Marshall, “Simulation of Pile-up in the ATLAS Experiment,” *J. Phys. Conf. Ser.* **513** (2014) 022024.
- [98] “First beam in the LHC - accelerating science,”, <https://home.cern/news/news/accelerators/record-luminosity-well-done-lhc>. Accessed: 2021-01-10.
- [99] **ATLAS Collaboration** Collaboration, “Luminosity determination in  $pp$  collisions at  $\sqrt{s} = 13$  TeV using the ATLAS detector at the LHC,” Tech. Rep. ATLAS-CONF-2019-021, CERN, Geneva, Jun, 2019. <https://cds.cern.ch/record/2677054>.
- [100] **ATLAS** Collaboration, M. Aaboud *et al.*, “Luminosity determination in  $pp$  collisions at  $\sqrt{s} = 8$  TeV using the ATLAS detector at the LHC,” *Eur. Phys. J. C* **76** no. 12, (2016) 653, [arXiv:1608.03953 \[hep-ex\]](https://arxiv.org/abs/1608.03953).
- [101] G. Avoni, M. Bruschi, G. Cabras, D. Caforio, N. Dehghanian, A. Floderus, B. Giacobbe, F. Giannuzzi, F. Giorgi, P. Grafström, V. Hedberg, F. L. Manghi, S. Meneghini, J. Pinfold, E. Richards, C. Sbarra, N. S. Cesari, A. Sbrizzi, R. Soluk, G. Ucchielli, S. Valentinetto, O. Viazlo, M. Villa, C. Vittori, R. Vuillermet, and A. Zoccoli, “The new LUCID-2 detector for luminosity measurement and monitoring in ATLAS,” *Journal of Instrumentation* **13** no. 07, (Jul, 2018) P07017–P07017. <https://doi.org/10.1088/1748-0221/13/07/p07017>.
- [102] S. van der Meer, “Calibration of the effective beam height in the ISR,” Tech. Rep. CERN-ISR-PO-68-31. ISR-PO-68-31, CERN, Geneva, 1968. <https://cds.cern.ch/record/296752>.
- [103] P. Grafström and W. Kozanecki, “Luminosity determination at proton colliders,” *Progress in Particle and Nuclear Physics* **81** (2015) 97 – 148. <http://www.sciencedirect.com/science/article/pii/S0146641014000878>.
- [104] “New schedule for CERN’s accelerators and experiments,”. <https://home.cern/news/press-release/cern/first-beam-lhc-accelerating-science>. Accessed: 2021-01-10.
- [105] **ATLAS** Collaboration, G. Aad *et al.*, “Luminosity Determination in  $pp$  Collisions at  $\sqrt{s} = 7$  TeV Using the ATLAS Detector at the LHC,” *Eur. Phys. J. C* **71** (2011) 1630, [arXiv:1101.2185 \[hep-ex\]](https://arxiv.org/abs/1101.2185).
- [106] **ATLAS Collaboration** Collaboration, G. Aad *et al.*, “Improved luminosity determination in  $pp$  collisions at  $\sqrt{s} = 7$  TeV using the ATLAS detector at the LHC. Improved luminosity determination in  $pp$  collisions at  $\sqrt{s} = 7$  TeV using the ATLAS detector at the LHC,” *Eur. Phys. J. C* **73** no. CERN-PH-EP-2013-026. CERN-PH-EP-2013-026, (Feb, 2013) 2518. 27 p. <https://cds.cern.ch/record/1517411>.

- Comments: 26 pages plus author list (39 pages total), 17 figures, 9 tables, submitted to EPJC, All figures are available at <a href=.
- [107] “Record luminosity: well done LHC,”. <https://home.cern/news/news/accelerators/new-schedule-cerns-accelerators-and-experiments>. Accessed: 2021-01-10.
- [108] A. G., B. A. I., B. O., F. P., L. M., R. L., and T. L., *High-Luminosity Large Hadron Collider (HL-LHC): Technical Design Report V. 0.1*. CERN Yellow Reports: Monographs. CERN, Geneva, 2017. <https://cds.cern.ch/record/2284929>.
- [109] J. Pequenao, “Computer generated image of the whole ATLAS detector.” Mar, 2008.
- [110] **ATLAS** Collaboration, “ATLAS: Detector and physics performance technical design report. Volume 1.”.
- [111] J. Pequenao, “Computer generated image of the ATLAS inner detector.” Mar, 2008.
- [112] **ATLAS Collaboration** Collaboration, K. Potamianos, “The upgraded Pixel detector and the commissioning of the Inner Detector tracking of the ATLAS experiment for Run-2 at the Large Hadron Collider,” Tech. Rep. ATL-PHYS-PROC-2016-104, CERN, Geneva, Aug, 2016. <https://cds.cern.ch/record/2209070>. 15 pages, EPS-HEP 2015 Proceedings.
- [113] **ATLAS IBL** Collaboration, B. Abbott *et al.*, “Production and Integration of the ATLAS Insertable B-Layer,” *JINST* **13** no. 05, (2018) T05008, [arXiv:1803.00844 \[physics.ins-det\]](https://arxiv.org/abs/1803.00844).
- [114] **ATLAS** Collaboration, “ATLAS Insertable B-Layer Technical Design Report,” Tech. Rep. CERN-LHCC-2010-013. ATLAS-TDR-19, Sep, 2010. <http://cds.cern.ch/record/1291633>.
- [115] **ATLAS** Collaboration, G. Aad *et al.*, “ATLAS b-jet identification performance and efficiency measurement with  $t\bar{t}$  events in pp collisions at  $\sqrt{s} = 13$  TeV,” *Eur. Phys. J. C* **79** no. 11, (2019) 970, [arXiv:1907.05120 \[hep-ex\]](https://arxiv.org/abs/1907.05120).
- [116] ATLAS Collaboration, “Particle Identification Performance of the ATLAS Transition Radiation Tracker.” ATLAS-CONF-2011-128, 2011. <https://cds.cern.ch/record/1383793>.
- [117] J. Pequenao, “Computer Generated image of the ATLAS calorimeter.” Mar, 2008.
- [118] J. Pequenao, “Computer generated image of the ATLAS Muons subsystem.” Mar, 2008.
- [119] S. Lee, M. Livan, and R. Wigmans, “Dual-Readout Calorimetry,” *Rev. Mod. Phys.* **90** no. arXiv:1712.05494. 2, (Dec, 2017) 025002. 40 p. <https://cds.cern.ch/record/2637852>. 44 pages, 53 figures, accepted for publication in Review of Modern Physics.
- [120] M. Leite, “Performance of the ATLAS Zero Degree Calorimeter,” Tech. Rep. ATL-FWD-PROC-2013-001, CERN, Geneva, Nov, 2013. <https://cds.cern.ch/record/1628749>.
- [121] S. Abdel Khalek *et al.*, “The ALFA Roman Pot Detectors of ATLAS,” *JINST* **11** no. 11, (2016) P11013, [arXiv:1609.00249 \[physics.ins-det\]](https://arxiv.org/abs/1609.00249).

- [122] U. Amaldi, G. Cocconi, A. Diddens, R. Dobinson, J. Dorenbosch, W. Duinker, D. Gustavson, J. Meyer, K. Potter, A. Wetherell, A. Baroncelli, and C. Bosio, “The real part of the forward proton proton scattering amplitude measured at the cern intersecting storage rings,” *Physics Letters B* **66** no. 4, (1977) 390 – 394.  
<http://www.sciencedirect.com/science/article/pii/0370269377900223>.
- [123] L. Adamczyk, E. Banaś, A. Brandt, M. Bruschi, S. Grinstein, J. Lange, M. Rijssenbeek, P. Sicho, R. Staszewski, T. Sykora, M. Trzebiński, J. Chwastowski, and K. Korcyl, “Technical Design Report for the ATLAS Forward Proton Detector,” Tech. Rep. CERN-LHCC-2015-009. ATLAS-TDR-024, May, 2015.  
<https://cds.cern.ch/record/2017378>.
- [124] **ATLAS** Collaboration, A. R. Martínez, “The Run-2 ATLAS Trigger System,” *J. Phys. Conf. Ser.* **762** no. 1, (2016) 012003.
- [125] **ATLAS Collaboration** Collaboration, *ATLAS level-1 trigger: Technical Design Report*. Technical Design Report ATLAS. CERN, Geneva, 1998.  
<https://cds.cern.ch/record/381429>.
- [126] **ATLAS Collaboration** Collaboration, P. Jenni, M. Nessi, M. Nordberg, and K. Smith, *ATLAS high-level trigger, data-acquisition and controls: Technical Design Report*. Technical Design Report ATLAS. CERN, Geneva, 2003.  
<https://cds.cern.ch/record/616089>.
- [127] **ATLAS** Collaboration, G. Aad *et al.*, “The ATLAS Simulation Infrastructure,” *Eur. Phys. J. C* **70** (2010) 823–874, [arXiv:1005.4568 \[physics.ins-det\]](https://arxiv.org/abs/1005.4568).
- [128] T. Gleisberg, S. Hoeche, F. Krauss, M. Schonherr, S. Schumann, F. Siegert, and J. Winter, “Event generation with SHERPA 1.1,” *JHEP* **02** (2009) 007, [arXiv:0811.4622 \[hep-ph\]](https://arxiv.org/abs/0811.4622).
- [129] A. Buckley *et al.*, “General-purpose event generators for LHC physics,” *Phys. Rept.* **504** (2011) 145–233, [arXiv:1101.2599 \[hep-ph\]](https://arxiv.org/abs/1101.2599).
- [130] V. N. Gribov and L. N. Lipatov, “Deep inelastic e p scattering in perturbation theory,” *Sov. J. Nucl. Phys.* **15** (1972) 438–450.
- [131] J. Blumlein, T. Doyle, F. Hautmann, M. Klein, and A. Vogt, “Structure functions in deep inelastic scattering at HERA,” in *Workshop on Future Physics at HERA (To be followed by meetings 7-9 Feb and 30-31 May 1996 at DESY)*. 9, 1996. [arXiv:hep-ph/9609425](https://arxiv.org/abs/hep-ph/9609425).
- [132] A. Buckley, J. Ferrando, S. Lloyd, K. Nordström, B. Page, M. Rüfenacht, M. Schönher, and G. Watt, “LHAPDF6: parton density access in the LHC precision era,” *Eur. Phys. J. C* **75** (2015) 132, [arXiv:1412.7420 \[hep-ph\]](https://arxiv.org/abs/1412.7420).
- [133] M. Bengtsson and T. Sjostrand, “Coherent Parton Showers Versus Matrix Elements: Implications of PETRA - PEP Data,” *Phys. Lett. B* **185** (1987) 435.
- [134] S. Catani, F. Krauss, R. Kuhn, and B. R. Webber, “QCD matrix elements + parton showers,” *JHEP* **11** (2001) 063, [arXiv:hep-ph/0109231](https://arxiv.org/abs/hep-ph/0109231).
- [135] L. Lonnblad, “Correcting the color dipole cascade model with fixed order matrix elements,” *JHEP* **05** (2002) 046, [arXiv:hep-ph/0112284](https://arxiv.org/abs/hep-ph/0112284).
- [136] B. Andersson, G. Gustafson, G. Ingelman, and T. Sjostrand, “Parton Fragmentation and String Dynamics,” *Phys. Rept.* **97** (1983) 31–145.

- [137] B. Andersson, *The Lund Model*. Cambridge Monographs on Particle Physics, Nuclear Physics and Cosmology. Cambridge University Press, 1998.
- [138] D. Amati and G. Veneziano, “Preconfinement as a Property of Perturbative QCD,” *Phys. Lett. B* **83** (1979) 87–92.
- [139] M. Dobbs and J. B. Hansen, “The HepMC C++ Monte Carlo event record for High Energy Physics,” *Comput. Phys. Commun.* **134** (2001) 41–46.
- [140] **GEANT4** Collaboration, S. Agostinelli *et al.*, “GEANT4: A Simulation toolkit,” *Nucl. Instrum. Meth. A* **506** (2003) 250–303.
- [141] **ATLAS Collaboration** Collaboration, “The new Fast Calorimeter Simulation in ATLAS,” Tech. Rep. ATL-SOFT-PUB-2018-002, CERN, Geneva, Jul, 2018. <https://cds.cern.ch/record/2630434>.
- [142] K. Cranmer, “Practical Statistics for the LHC,” in *2011 European School of High-Energy Physics*, pp. 267–308. 2014. [arXiv:1503.07622 \[physics.data-an\]](https://arxiv.org/abs/1503.07622).
- [143] G. Cowan, K. Cranmer, E. Gross, and O. Vitells, “Asymptotic formulae for likelihood-based tests of new physics,” *Eur. Phys. J. C* **71** (2011) 1554, [arXiv:1007.1727 \[physics.data-an\]](https://arxiv.org/abs/1007.1727). [Erratum: Eur. Phys. J.C73,2501(2013)].
- [144] ATLAS Collaboration, “Reproduction searches for new physics with the ATLAS experiment through publication of full statistical likelihoods.” ATL-PHYS-PUB-2019-029, 2019. <https://cds.cern.ch/record/2684863>.
- [145] **ROOT Collaboration** Collaboration, K. Cranmer, G. Lewis, L. Moneta, A. Shibata, and W. Verkerke, “HistFactory: A tool for creating statistical models for use with RooFit and RooStats,” Tech. Rep. CERN-OPEN-2012-016, New York U., New York, Jan, 2012. <https://cds.cern.ch/record/1456844>.
- [146] W. Verkerke and D. P. Kirkby, “The RooFit toolkit for data modeling,” *eConf C0303241* (2003) MOLT007, [arXiv:physics/0306116 \[physics\]](https://arxiv.org/abs/physics/0306116). [,186(2003)].
- [147] L. Moneta, K. Belasco, K. S. Cranmer, S. Kreiss, A. Lazzaro, D. Piparo, G. Schott, W. Verkerke, and M. Wolf, “The RooStats Project,” *PoS ACAT2010* (2010) 057, [arXiv:1009.1003 \[physics.data-an\]](https://arxiv.org/abs/1009.1003).
- [148] F. James and M. Roos, “MINUIT: a system for function minimization and analysis of the parameter errors and corrections,” *Comput. Phys. Commun.* **10** no. CERN-DD-75-20, (Jul, 1975) 343–367. 38 p. <https://cds.cern.ch/record/310399>.
- [149] R. Brun and F. Rademakers, “ROOT: An object oriented data analysis framework,” *Nucl. Instrum. Meth. A* **389** (1997) 81–86.
- [150] I. Antcheva *et al.*, “Root — a c++ framework for petabyte data storage, statistical analysis and visualization,” *Computer Physics Communications* **182** no. 6, (2011) 1384 – 1385. <http://www.sciencedirect.com/science/article/pii/S0010465511000701>.
- [151] M. Baak, G. J. Besjes, D. Côte, A. Koutsman, J. Lorenz, and D. Short, “HistFitter software framework for statistical data analysis,” *Eur. Phys. J. C* **75** (2015) 153, [arXiv:1410.1280 \[hep-ex\]](https://arxiv.org/abs/1410.1280).
- [152] L. Heinrich, M. Feickert, G. Stark, and K. Cranmer, “pyhf: pure-python implementation of histfactory statistical models,” *Journal of Open Source Software* **6** no. 58, (2021) 2823. <https://doi.org/10.21105/joss.02823>.

- [153] L. Heinrich, M. Feickert, and G. Stark, “pyhf: v0.6.0.” <https://github.com/scikit-hep/pyhf>.
- [154] A. Paszke, S. Gross, F. Massa, A. Lerer, J. Bradbury, G. Chanan, T. Killeen, Z. Lin, N. Gimelshein, L. Antiga, A. Desmaison, A. Kopf, E. Yang, Z. DeVito, M. Raison, A. Tejani, S. Chilamkurthy, B. Steiner, L. Fang, J. Bai, and S. Chintala, “Pytorch: An imperative style, high-performance deep learning library,” in *Advances in Neural Information Processing Systems 32*, H. Wallach, H. Larochelle, A. Beygelzimer, F. d’Alché-Buc, E. Fox, and R. Garnett, eds., pp. 8024–8035. Curran Associates, Inc., 2019. <http://papers.neurips.cc/paper/9015-pytorch-an-imperative-style-high-performance-deep-learning-library.pdf>.
- [155] M. Abadi, A. Agarwal, P. Barham, E. Brevdo, Z. Chen, C. Citro, G. S. Corrado, A. Davis, J. Dean, M. Devin, S. Ghemawat, I. Goodfellow, A. Harp, G. Irving, M. Isard, Y. Jia, R. Jozefowicz, L. Kaiser, M. Kudlur, J. Levenberg, D. Mané, R. Monga, S. Moore, D. Murray, C. Olah, M. Schuster, J. Shlens, B. Steiner, I. Sutskever, K. Talwar, P. Tucker, V. Vanhoucke, V. Vasudevan, F. Viégas, O. Vinyals, P. Warden, M. Wattenberg, M. Wicke, Y. Yu, and X. Zheng, “TensorFlow: Large-scale machine learning on heterogeneous systems,” 2015. <https://www.tensorflow.org/>. Software available from tensorflow.org.
- [156] J. Bradbury, R. Frostig, P. Hawkins, M. J. Johnson, C. Leary, D. Maclaurin, and S. Wanderman-Milne, “JAX: composable transformations of Python+NumPy programs,” 2018. <http://github.com/google/jax>.
- [157] A. Wald, “Tests of statistical hypotheses concerning several parameters when the number of observations is large,” *Transactions of the American Mathematical Society* **54** no. 3, (1943) 426–482. <https://doi.org/10.1090/S0002-9947-1943-0012401-3>.
- [158] S. S. Wilks, “The large-sample distribution of the likelihood ratio for testing composite hypotheses,” *Ann. Math. Statist.* **9** no. 1, (03, 1938) 60–62. <https://doi.org/10.1214/aoms/1177732360>.
- [159] G. Cowan, “Statistics for Searches at the LHC,” in *69th Scottish Universities Summer School in Physics: LHC Physics*, pp. 321–355. 7, 2013. [arXiv:1307.2487 \[hep-ex\]](https://arxiv.org/abs/1307.2487).
- [160] A. L. Read, “Presentation of search results: the  $CL_S$  technique,” *J. Phys. G* **28** (2002) 2693.
- [161] R. D. Cousins, J. T. Linnemann, and J. Tucker, “Evaluation of three methods for calculating statistical significance when incorporating a systematic uncertainty into a test of the background-only hypothesis for a Poisson process,” *Nucl. Instrum. Meth. A* **595** no. 2, (2008) 480, [arXiv:physics/0702156 \[physics.data-an\]](https://arxiv.org/abs/physics/0702156).
- [162] K. CRANMER, “Statistical challenges for searches for new physics at the lhc,” *Statistical Problems in Particle Physics, Astrophysics and Cosmology* (May, 2006) . [http://dx.doi.org/10.1142/9781860948985\\_0026](http://dx.doi.org/10.1142/9781860948985_0026).
- [163] ATLAS Collaboration, “Search for direct pair production of a chargino and a neutralino decaying to the 125 GeV Higgs boson in  $\sqrt{s} = 8$  TeV  $pp$  collisions with the ATLAS detector,” *Eur. Phys. J. C* **75** (2015) 208, [arXiv:1501.07110 \[hep-ex\]](https://arxiv.org/abs/1501.07110).
- [164] ATLAS Collaboration, “Search for chargino and neutralino production in final states with a Higgs boson and missing transverse momentum at  $\sqrt{s} = 13$  TeV with the ATLAS detector,” *Phys. Rev. D* **100** (2019) 012006, [arXiv:1812.09432 \[hep-ex\]](https://arxiv.org/abs/1812.09432).

- [165] CMS Collaboration, “Search for electroweak production of charginos and neutralinos in  $W H$  events in proton–proton collisions at  $\sqrt{s} = 13$  TeV,” *JHEP* **11** (2017) 029, [arXiv:1706.09933 \[hep-ex\]](https://arxiv.org/abs/1706.09933).
- [166] ATLAS Collaboration, “Search for direct production of electroweakinos in final states with one lepton, missing transverse momentum and a Higgs boson decaying into two  $b$ -jets in  $pp$  collisions at  $\sqrt{s} = 13$  TeV with the ATLAS detector,” *Eur. Phys. J. C* **80** (2020) 691, [arXiv:1909.09226 \[hep-ex\]](https://arxiv.org/abs/1909.09226).
- [167] ATLAS Collaboration, “Improvements in  $t\bar{t}$  modelling using NLO+PS Monte Carlo generators for Run 2.” ATL-PHYS-PUB-2018-009, 2018. <https://cds.cern.ch/record/2630327>.
- [168] ATLAS Collaboration, “Modelling of the  $t\bar{t}H$  and  $t\bar{t}V(V = W, Z)$  processes for  $\sqrt{s} = 13$  TeV ATLAS analyses.” ATL-PHYS-PUB-2016-005, 2016. <https://cds.cern.ch/record/2120826>.
- [169] ATLAS Collaboration, “ATLAS simulation of boson plus jets processes in Run 2.” ATL-PHYS-PUB-2017-006, 2017. <https://cds.cern.ch/record/2261937>.
- [170] ATLAS Collaboration, “Multi-Boson Simulation for 13 TeV ATLAS Analyses.” ATL-PHYS-PUB-2017-005, 2017. <https://cds.cern.ch/record/2261933>.
- [171] J. Alwall, R. Frederix, S. Frixione, V. Hirschi, F. Maltoni, O. Mattelaer, H. S. Shao, T. Stelzer, P. Torrielli, and M. Zaro, “The automated computation of tree-level and next-to-leading order differential cross sections, and their matching to parton shower simulations,” *JHEP* **07** (2014) 079, [arXiv:1405.0301 \[hep-ph\]](https://arxiv.org/abs/1405.0301).
- [172] R. Frederix and S. Frixione, “Merging meets matching in MC@NLO,” *JHEP* **12** (2012) 061, [arXiv:1209.6215 \[hep-ph\]](https://arxiv.org/abs/1209.6215).
- [173] T. Sjöstrand, S. Ask, J. R. Christiansen, R. Corke, N. Desai, P. Ilten, S. Mrenna, S. Prestel, C. O. Rasmussen, and P. Z. Skands, “An Introduction to PYTHIA 8.2,” *Comput. Phys. Commun.* **191** (2015) 159–177, [arXiv:1410.3012 \[hep-ph\]](https://arxiv.org/abs/1410.3012).
- [174] L. Lönnblad and S. Prestel, “Matching tree-level matrix elements with interleaved showers,” *JHEP* **03** (2012) 019, [arXiv:1109.4829 \[hep-ph\]](https://arxiv.org/abs/1109.4829).
- [175] R. D. Ball *et al.*, “Parton distributions with LHC data,” *Nucl. Phys. B* **867** (2013) 244, [arXiv:1207.1303 \[hep-ph\]](https://arxiv.org/abs/1207.1303).
- [176] ATLAS Collaboration, “ATLAS Pythia 8 tunes to 7 TeV data.” ATL-PHYS-PUB-2014-021, 2014. <https://cds.cern.ch/record/1966419>.
- [177] D. J. Lange, “The EvtGen particle decay simulation package,” *Nucl. Instrum. Meth. A* **462** (2001) 152.
- [178] ATLAS Collaboration, “The Pythia 8 A3 tune description of ATLAS minimum bias and inelastic measurements incorporating the Donnachie–Landshoff diffractive model.” ATL-PHYS-PUB-2016-017, 2016. <https://cds.cern.ch/record/2206965>.
- [179] B. Fuks, M. Klasen, D. R. Lamprea, and M. Rothberg, “Precision predictions for electroweak superpartner production at hadron colliders with RESUMMINO,” *Eur. Phys. J. C* **73** (2013) 2480, [arXiv:1304.0790 \[hep-ph\]](https://arxiv.org/abs/1304.0790).

- [180] J. Fiaschi and M. Klasen, “Neutralino-chargino pair production at NLO+NLL with resummation-improved parton density functions for LHC Run II,” *Phys. Rev. D* **98** no. 5, (2018) 055014, [arXiv:1805.11322 \[hep-ph\]](https://arxiv.org/abs/1805.11322).
- [181] B. Fuks, M. Klasen, D. R. Lamprea, and M. Rothenberg, “Gaugino production in proton-proton collisions at a center-of-mass energy of 8 TeV,” *JHEP* **10** (2012) 081, [arXiv:1207.2159 \[hep-ph\]](https://arxiv.org/abs/1207.2159).
- [182] S. Alioli, P. Nason, C. Oleari, and E. Re, “A general framework for implementing NLO calculations in shower Monte Carlo programs: the POWHEG BOX,” *JHEP* **06** (2010) 043, [arXiv:1002.2581 \[hep-ph\]](https://arxiv.org/abs/1002.2581).
- [183] S. Frixione, P. Nason, and G. Ridolfi, “A Positive-weight next-to-leading-order Monte Carlo for heavy flavour hadroproduction,” *JHEP* **09** (2007) 126, [arXiv:0707.3088 \[hep-ph\]](https://arxiv.org/abs/0707.3088).
- [184] P. Nason, “A New method for combining NLO QCD with shower Monte Carlo algorithms,” *JHEP* **11** (2004) 040, [arXiv:hep-ph/0409146](https://arxiv.org/abs/hep-ph/0409146).
- [185] E. Bothmann *et al.*, “Event generation with Sherpa 2.2,” *SciPost Phys.* **7** no. 3, (2019) 034, [arXiv:1905.09127 \[hep-ph\]](https://arxiv.org/abs/1905.09127).
- [186] S. Höche, F. Krauss, S. Schumann, and F. Siegert, “QCD matrix elements and truncated showers,” *JHEP* **05** (2009) 053, [arXiv:0903.1219 \[hep-ph\]](https://arxiv.org/abs/0903.1219).
- [187] S. Höche, F. Krauss, M. Schönher, and F. Siegert, “QCD matrix elements + parton showers. The NLO case,” *JHEP* **04** (2013) 027, [arXiv:1207.5030 \[hep-ph\]](https://arxiv.org/abs/1207.5030).
- [188] NNPDF Collaboration, R. D. Ball *et al.*, “Parton distributions for the LHC run II,” *JHEP* **04** (2015) 040, [arXiv:1410.8849 \[hep-ph\]](https://arxiv.org/abs/1410.8849).
- [189] ATLAS Collaboration, “Example ATLAS tunes of PYTHIA8, PYTHIA6 and POWHEG to an observable sensitive to  $Z$  boson transverse momentum.” ATL-PHYS-PUB-2013-017, 2013. <https://cds.cern.ch/record/1629317>.
- [190] M. Czakon and A. Mitov, “Top++: A program for the calculation of the top-pair cross-section at hadron colliders,” *Comput. Phys. Commun.* **185** (2014) 2930, [arXiv:1112.5675 \[hep-ph\]](https://arxiv.org/abs/1112.5675).
- [191] M. Cacciari, M. Czakon, M. Mangano, A. Mitov, and P. Nason, “Top-pair production at hadron colliders with next-to-next-to-leading logarithmic soft-gluon resummation,” *Phys. Lett. B* **710** (2012) 612–622, [arXiv:1111.5869 \[hep-ph\]](https://arxiv.org/abs/1111.5869).
- [192] P. Kant, O. M. Kind, T. Kintscher, T. Lohse, T. Martini, S. Mölbitz, P. Rieck, and P. Uwer, “HatHor for single top-quark production: Updated predictions and uncertainty estimates for single top-quark production in hadronic collisions,” *Comput. Phys. Commun.* **191** (2015) 74–89, [arXiv:1406.4403 \[hep-ph\]](https://arxiv.org/abs/1406.4403).
- [193] N. Kidonakis, “Two-loop soft anomalous dimensions for single top quark associated production with a  $W^-$  or  $H^-$ ,” *Phys. Rev. D* **82** (2010) 054018, [arXiv:1005.4451 \[hep-ph\]](https://arxiv.org/abs/1005.4451).
- [194] J. M. Campbell and R. K. Ellis, “ $t\bar{t}W^{+-}$  production and decay at NLO,” *JHEP* **07** (2012) 052, [arXiv:1204.5678 \[hep-ph\]](https://arxiv.org/abs/1204.5678).

- [195] A. Lazopoulos, T. McElmurry, K. Melnikov, and F. Petriello, “Next-to-leading order QCD corrections to  $t\bar{t}Z$  production at the LHC,” *Phys. Lett. B* **666** (2008) 62–65, [arXiv:0804.2220 \[hep-ph\]](https://arxiv.org/abs/0804.2220).
- [196] R. Gavin, Y. Li, F. Petriello, and S. Quackenbush, “FEWZ 2.0: A code for hadronic  $Z$  production at next-to-next-to-leading order,” [arXiv:1011.3540 \[hep-ph\]](https://arxiv.org/abs/1011.3540).
- [197] **LHC Higgs Cross Section Working Group** Collaboration, D. de Florian *et al.*, “Handbook of LHC Higgs Cross Sections: 4. Deciphering the Nature of the Higgs Sector,” [arXiv:1610.07922 \[hep-ph\]](https://arxiv.org/abs/1610.07922).
- [198] ATLAS Collaboration, “Performance of the ATLAS track reconstruction algorithms in dense environments in LHC Run 2,” *Eur. Phys. J. C* **77** (2017) 673, [arXiv:1704.07983 \[hep-ex\]](https://arxiv.org/abs/1704.07983).
- [199] R. Frühwirth, “Application of Kalman filtering to track and vertex fitting,” *Nucl. Instrum. Methods Phys. Res., A* **262** no. HEPHY-PUB-503, (Jun, 1987) 444. 19 p. <https://cds.cern.ch/record/178627>.
- [200] T. Cornelissen, M. Elsing, I. Gavrilenco, W. Liebig, E. Moyse, and A. Salzburger, “The new ATLAS track reconstruction (NEWT),” *J. Phys.: Conf. Ser.* **119** (2008) 032014. <https://cds.cern.ch/record/1176900>.
- [201] ATLAS Collaboration, “Vertex Reconstruction Performance of the ATLAS Detector at  $\sqrt{s} = 13$  TeV.” ATL-PHYS-PUB-2015-026, 2015. <https://cds.cern.ch/record/2037717>.
- [202] ATLAS Collaboration, “Reconstruction of primary vertices at the ATLAS experiment in Run 1 proton–proton collisions at the LHC,” *Eur. Phys. J. C* **77** (2017) 332, [arXiv:1611.10235 \[hep-ex\]](https://arxiv.org/abs/1611.10235).
- [203] ATLAS Collaboration, “Topological cell clustering in the ATLAS calorimeters and its performance in LHC Run 1,” *Eur. Phys. J. C* **77** (2017) 490, [arXiv:1603.02934 \[hep-ex\]](https://arxiv.org/abs/1603.02934).
- [204] ATLAS Collaboration, “Electron and photon performance measurements with the ATLAS detector using the 2015–2017 LHC proton–proton collision data,” *JINST* **14** (2019) P12006, [arXiv:1908.00005 \[hep-ex\]](https://arxiv.org/abs/1908.00005).
- [205] ATLAS Collaboration, “Measurement of the photon identification efficiencies with the ATLAS detector using LHC Run 2 data collected in 2015 and 2016,” *Eur. Phys. J. C* **79** (2019) 205, [arXiv:1810.05087 \[hep-ex\]](https://arxiv.org/abs/1810.05087).
- [206] ATLAS Collaboration, “Electron and photon energy calibration with the ATLAS detector using 2015–2016 LHC proton–proton collision data,” *JINST* **14** (2019) P03017, [arXiv:1812.03848 \[hep-ex\]](https://arxiv.org/abs/1812.03848).
- [207] ATLAS Collaboration, “Electron reconstruction and identification in the ATLAS experiment using the 2015 and 2016 LHC proton–proton collision data at  $\sqrt{s} = 13$  TeV,” *Eur. Phys. J. C* **79** (2019) 639, [arXiv:1902.04655 \[hep-ex\]](https://arxiv.org/abs/1902.04655).
- [208] ATLAS Collaboration, “Muon reconstruction performance of the ATLAS detector in proton–proton collision data at  $\sqrt{s} = 13$  TeV,” *Eur. Phys. J. C* **76** (2016) 292, [arXiv:1603.05598 \[hep-ex\]](https://arxiv.org/abs/1603.05598).

- [209] **ATLAS** Collaboration, “Muon reconstruction and identification efficiency in ATLAS using the full Run 2  $pp$  collision data set at  $\sqrt{s} = 13$  TeV,” [arXiv:2012.00578 \[hep-ex\]](https://arxiv.org/abs/2012.00578).
- [210] M. Cacciari, G. P. Salam, and G. Soyez, “The anti- $k_t$  jet clustering algorithm,” *JHEP* **04** (2008) 063, [arXiv:0802.1189 \[hep-ph\]](https://arxiv.org/abs/0802.1189).
- [211] M. Cacciari, G. P. Salam, and G. Soyez, “FastJet user manual,” *Eur. Phys. J. C* **72** (2012) 1896, [arXiv:1111.6097 \[hep-ph\]](https://arxiv.org/abs/1111.6097).
- [212] M. Cacciari, “FastJet: A Code for fast  $k_t$  clustering, and more,” in *Deep inelastic scattering. Proceedings, 14th International Workshop, DIS 2006, Tsukuba, Japan, April 20-24, 2006*, pp. 487–490. 2006. [arXiv:hep-ph/0607071 \[hep-ph\]](https://arxiv.org/abs/hep-ph/0607071). [,125(2006)].
- [213] **ATLAS** Collaboration, G. Aad *et al.*, “Jet energy scale and resolution measured in proton-proton collisions at  $\sqrt{s} = 13$  TeV with the ATLAS detector,” [arXiv:2007.02645 \[hep-ex\]](https://arxiv.org/abs/2007.02645).
- [214] M. Cacciari and G. P. Salam, “Pileup subtraction using jet areas,” *Phys. Lett. B* **659** (2008) 119–126, [arXiv:0707.1378 \[hep-ph\]](https://arxiv.org/abs/0707.1378).
- [215] ATLAS Collaboration, “Jet energy measurement with the ATLAS detector in proton–proton collisions at  $\sqrt{s} = 7$  TeV,” *Eur. Phys. J. C* **73** (2013) 2304, [arXiv:1112.6426 \[hep-ex\]](https://arxiv.org/abs/1112.6426).
- [216] ATLAS Collaboration, “Determination of jet calibration and energy resolution in proton–proton collisions at  $\sqrt{s} = 8$  TeV using the ATLAS detector,” [arXiv:1910.04482 \[hep-ex\]](https://arxiv.org/abs/1910.04482).
- [217] ATLAS Collaboration, “Performance of pile-up mitigation techniques for jets in  $pp$  collisions at  $\sqrt{s} = 8$  TeV using the ATLAS detector,” *Eur. Phys. J. C* **76** (2016) 581, [arXiv:1510.03823 \[hep-ex\]](https://arxiv.org/abs/1510.03823).
- [218] ATLAS Collaboration, “Optimisation and performance studies of the ATLAS  $b$ -tagging algorithms for the 2017-18 LHC run.” ATL-PHYS-PUB-2017-013, 2017. <https://cds.cern.ch/record/2273281>.
- [219] ATLAS Collaboration, “ATLAS  $b$ -jet identification performance and efficiency measurement with  $t\bar{t}$  events in  $pp$  collisions at  $\sqrt{s} = 13$  TeV,” *Eur. Phys. J. C* **79** (2019) 970, [arXiv:1907.05120 \[hep-ex\]](https://arxiv.org/abs/1907.05120).
- [220] ATLAS Collaboration, “Measurements of  $b$ -jet tagging efficiency with the ATLAS detector using  $t\bar{t}$  events at  $\sqrt{s} = 13$  TeV,” *JHEP* **08** (2018) 089, [arXiv:1805.01845 \[hep-ex\]](https://arxiv.org/abs/1805.01845).
- [221] ATLAS Collaboration, “Performance of missing transverse momentum reconstruction with the ATLAS detector using proton–proton collisions at  $\sqrt{s} = 13$  TeV,” *Eur. Phys. J. C* **78** (2018) 903, [arXiv:1802.08168 \[hep-ex\]](https://arxiv.org/abs/1802.08168).
- [222] **ATLAS Collaboration** Collaboration, “ $E_T^{\text{miss}}$  performance in the ATLAS detector using 2015-2016 LHC p-p collisions,” Tech. Rep. ATLAS-CONF-2018-023, CERN, Geneva, Jun, 2018. [http://cds.cern.ch/record/2625233](https://cds.cern.ch/record/2625233).
- [223] D. Adams *et al.*, “Recommendations of the Physics Objects and Analysis Harmonisation Study Groups 2014,” Tech. Rep. ATL-PHYS-INT-2014-018, CERN, Geneva, Jul, 2014. <https://cds.cern.ch/record/1743654>.

- [224] M. Cacciari, G. P. Salam, and G. Soyez, “The Catchment Area of Jets,” *JHEP* **04** (2008) 005, [arXiv:0802.1188 \[hep-ph\]](https://arxiv.org/abs/0802.1188).
- [225] **UA1** Collaboration, G. Arnison *et al.*, “Experimental Observation of Isolated Large Transverse Energy Electrons with Associated Missing Energy at  $\sqrt{s} = 540$  GeV,” *Phys. Lett. B* **122** (1983) 103–116.
- [226] **Aachen-Annecy-Birmingham-CERN-Helsinki-London(QMC)-Paris(CdF)-Riverside-Rome-Rutherford-Saclay(CEN)-Vienna** Collaboration, G. Arnison *et al.*, “Further evidence for charged intermediate vector bosons at the SPS collider,” *Phys. Lett. B* **129** no. CERN-EP-83-111, (Jun, 1985) 273–282. 17 p.  
<https://cds.cern.ch/record/163856>.
- [227] D. R. Tovey, “On measuring the masses of pair-produced semi-invisibly decaying particles at hadron colliders,” *JHEP* **04** (2008) 034, [arXiv:0802.2879 \[hep-ph\]](https://arxiv.org/abs/0802.2879).
- [228] G. Polesello and D. R. Tovey, “Supersymmetric particle mass measurement with the boost-corrected contransverse mass,” *JHEP* **03** (2010) 030, [arXiv:0910.0174 \[hep-ph\]](https://arxiv.org/abs/0910.0174).
- [229] **ATLAS** Collaboration, G. Aad *et al.*, “Performance of the missing transverse momentum triggers for the ATLAS detector during Run-2 data taking,” *JHEP* **08** (2020) 080, [arXiv:2005.09554 \[hep-ex\]](https://arxiv.org/abs/2005.09554).
- [230] **ATLAS** Collaboration, G. Aad *et al.*, “Performance of algorithms that reconstruct missing transverse momentum in  $\sqrt{s} = 8$  TeV proton-proton collisions in the ATLAS detector,” *Eur. Phys. J. C* **77** no. 4, (2017) 241, [arXiv:1609.09324 \[hep-ex\]](https://arxiv.org/abs/1609.09324).
- [231] ATLAS Collaboration, “ATLAS data quality operations and performance for 2015–2018 data-taking,” *JINST* **15** (2020) P04003, [arXiv:1911.04632 \[physics.ins-det\]](https://arxiv.org/abs/1911.04632).
- [232] ATLAS Collaboration, “Selection of jets produced in 13 TeV proton–proton collisions with the ATLAS detector.” ATLAS-CONF-2015-029, 2015.  
<https://cds.cern.ch/record/2037702>.
- [233] N. Hartmann, “ahoi.” <https://gitlab.com/nikoladze/ahoi>, 2018.
- [234] **ATLAS** Collaboration, “Object-based missing transverse momentum significance in the ATLAS detector,” Tech. Rep. ATLAS-CONF-2018-038, CERN, Geneva, Jul, 2018.  
<https://cds.cern.ch/record/2630948>.
- [235] A. Roodman, “Blind analysis in particle physics,” *eConf* **C030908** (2003) TUIT001, [arXiv:physics/0312102](https://arxiv.org/abs/physics/0312102).
- [236] ATLAS Collaboration, “A method for the construction of strongly reduced representations of ATLAS experimental uncertainties and the application thereof to the jet energy scale.” ATL-PHYS-PUB-2015-014, 2015. <https://cds.cern.ch/record/2037436>.
- [237] J. Bellm *et al.*, “Herwig 7.0/Herwig++ 3.0 release note,” *Eur. Phys. J. C* **76** no. 4, (2016) 196, [arXiv:1512.01178 \[hep-ph\]](https://arxiv.org/abs/1512.01178).
- [238] ATLAS Collaboration, “Simulation of top-quark production for the ATLAS experiment at  $\sqrt{s} = 13$  TeV.” ATL-PHYS-PUB-2016-004, 2016. <https://cds.cern.ch/record/2120417>.
- [239] S. Frixione, E. Laenen, P. Motylinski, C. White, and B. R. Webber, “Single-top hadroproduction in association with a  $W$  boson,” *JHEP* **07** (2008) 029, [arXiv:0805.3067 \[hep-ph\]](https://arxiv.org/abs/0805.3067).

- [240] **ATLAS Collaboration** Collaboration, “SUSY July 2020 Summary Plot Update,” Tech. Rep. ATL-PHYS-PUB-2020-020, CERN, Geneva, Jul, 2020.  
<http://cds.cern.ch/record/2725258>.
- [241] G. Apollinari, I. Béjar Alonso, O. Brüning, M. Lamont, and L. Rossi, *High-Luminosity Large Hadron Collider (HL-LHC): Preliminary Design Report*. CERN Yellow Reports: Monographs. CERN, Geneva, 2015. <https://cds.cern.ch/record/2116337>.
- [242] **LHC Reinterpretation Forum** Collaboration, W. Abdallah *et al.*, “Reinterpretation of LHC Results for New Physics: Status and Recommendations after Run 2,” *SciPost Phys.* **9** no. 2, (2020) 022, [arXiv:2003.07868 \[hep-ph\]](arXiv:2003.07868).
- [243] ATLAS Collaboration, “RECAST framework reinterpretation of an ATLAS Dark Matter Search constraining a model of a dark Higgs boson decaying to two  $b$ -quarks.” ATL-PHYS-PUB-2019-032, 2019. <https://cds.cern.ch/record/2686290>.
- [244] S. Ovyn, X. Rouby, and V. Lemaitre, “DELPHES, a framework for fast simulation of a generic collider experiment,” [arXiv:0903.2225 \[hep-ph\]](arXiv:0903.2225).
- [245] A. Buckley, J. Butterworth, D. Grellscheid, H. Hoeth, L. Lonnblad, J. Monk, H. Schulz, and F. Siegert, “Rivet user manual,” *Comput. Phys. Commun.* **184** (2013) 2803–2819, [arXiv:1003.0694 \[hep-ph\]](arXiv:1003.0694).
- [246] A. Buckley, D. Kar, and K. Nordström, “Fast simulation of detector effects in Rivet,” *SciPost Phys.* **8** (2020) 025, [arXiv:1910.01637 \[hep-ph\]](arXiv:1910.01637).
- [247] D. Dercks, N. Desai, J. S. Kim, K. Rolbiecki, J. Tattersall, and T. Weber, “CheckMATE 2: From the model to the limit,” *Comput. Phys. Commun.* **221** (2017) 383–418, [arXiv:1611.09856 \[hep-ph\]](arXiv:1611.09856).
- [248] M. Drees, H. Dreiner, D. Schmeier, J. Tattersall, and J. S. Kim, “CheckMATE: Confronting your Favourite New Physics Model with LHC Data,” *Comput. Phys. Commun.* **187** (2015) 227–265, [arXiv:1312.2591 \[hep-ph\]](arXiv:1312.2591).
- [249] E. Conte, B. Fuks, and G. Serret, “MadAnalysis 5, A User-Friendly Framework for Collider Phenomenology,” *Comput. Phys. Commun.* **184** (2013) 222–256, [arXiv:1206.1599 \[hep-ph\]](arXiv:1206.1599).
- [250] E. Maguire, L. Heinrich, and G. Watt, “HEPData: a repository for high energy physics data,” *J. Phys. Conf. Ser.* **898** no. 10, (2017) 102006, [arXiv:1704.05473 \[hep-ex\]](arXiv:1704.05473).
- [251] S. Kraml, S. Kulkarni, U. Laa, A. Lessa, W. Magerl, D. Proschofsky-Spindler, and W. Waltenberger, “SModelS: a tool for interpreting simplified-model results from the LHC and its application to supersymmetry,” *Eur. Phys. J. C* **74** (2014) 2868, [arXiv:1312.4175 \[hep-ph\]](arXiv:1312.4175).
- [252] F. Ambrogi, S. Kraml, S. Kulkarni, U. Laa, A. Lessa, V. Magerl, J. Sonneveld, M. Traub, and W. Waltenberger, “SModelS v1.1 user manual: Improving simplified model constraints with efficiency maps,” *Comput. Phys. Commun.* **227** (2018) 72–98, [arXiv:1701.06586 \[hep-ph\]](arXiv:1701.06586).
- [253] **ATLAS Collaboration**, “Search for direct production of electroweakinos in final states with one lepton, missing transverse momentum and a higgs boson decaying into two  $b$ -jets in  $pp$  collisions at  $\sqrt{s} = 13$  tev with the atlas detector,” 2021.  
<https://www.hepdata.net/record/ins1755298?version=4>.

- [254] **ATLAS** Collaboration, “1lbb-likelihoods-hepdata.tar.gz,” 2020.  
<https://www.hepdata.net/record/resource/1408476?view=true>.
- [255] K. Cranmer and I. Yavin, “RECAST: Extending the Impact of Existing Analyses,”  
*JHEP* **04** (2011) 038, [arXiv:1010.2506 \[hep-ex\]](https://arxiv.org/abs/1010.2506).